

Measurement of Something

by

Kiyotaka Akabori

Submitted in partial fulfillment of the

requirements for the degree of

Doctor of Philosophy

at

Carnegie Mellon University

Department of Physics

Pittsburgh, Pennsylvania

Advised by Professor John F. Nagle
and Professor Stephanie Tristram-Nagle

July 1, 2014

Contents

1	Introduction	1
2	Materials and Methods	3
2.1	X-ray optics	3
2.2	Hydration Chamber	3
2.3	Sample Preparation	4
2.3.1	Stock Solutions	4
2.3.2	Thin Film Samples	4
2.4	CCD detector	5
3	Structural Perturbation of Lipid Bilayers Due to Tat Peptide	6
3.1	Introduction	6
3.2	Materials and Methods	9
3.2.1	Volume Measurements	9
3.2.2	Analysis of Diffuse Scattering	11
3.2.3	Modeling the Bilayer Structure	17
3.2.4	Molecular Dynamics Simulation	23
3.3	Analysis of Molecular Dynamics Simulation Data	26
3.3.1	SIMtoEXP program	26
3.3.2	Local Thinning of Membranes	26
3.3.3	Lateral Decay Length of Membrane Thinning	28
3.4	Results	30
3.4.1	Bending and Bulk Modulus	30
3.4.2	Volume results	32
3.4.3	Electron Density Profile Modeling	33
3.4.4	Hard Wall Constrain Fits	43

3.4.5	Summary of Electron Density Profile Modeling	44
3.4.6	Molecular Dynamics Simulations	46
3.5	Discussion	55
3.6	Conclusion	58
4	Ripple Phase	60
4.1	Introduction	60
4.2	Materials and Methods	63
4.2.1	Sample Preparation	63
4.2.2	Instrumental Resolution	64
4.2.3	Low Angle X-ray Scattering Experiment	72
4.2.4	Near Grazing Incidence Wide Angle X-ray Scattering Experiment	74
4.2.5	Transmission Wide Angle X-ray Scattering Experiment . . .	76
4.3	LAXS: analysis	79
4.3.1	Lattice Structure	79
4.3.2	Sample q-space	80
4.3.3	Lorentz Correction	82
4.3.4	Absorption Correction for LAXS	87
4.3.5	Correction due to mosaic spread	91
4.4	LAXS: model	94
4.4.1	Contour Part of the Form Factor	94
4.4.2	Transbilayer Part of the Form Factor	94
4.5	LAXS: results	98
4.5.1	Data and Electron Density Profile	98
4.6	NGIWAXS: analysis	98
4.6.1	Absorption Correction	98
4.7	NGIWAXS: model	101
4.7.1	Thin rod model	101
4.8	NGIWAXS: results	101
4.9	TWAXS: results	101
4.10	Discussion	105
4.11	Conclusion	105
Appendices		106

A Tat	107
A.1 Analysis of Fixed Angle Data using NFIT	107
A.1.1 Theory	107
A.1.2 Results	107
A.2 Mosaic Spread for NFIT analysis	107
A.2.1 Mosaic Spread: Calculation	107
A.2.2 Mosaic Spread: Experiment	112
A.2.3 NFIT	114
A.2.4 Results	115
A.3 Some More Details of Tat Stuff if needed	115
B Ripple Phase	116
B.1 Derivation of the contour part of the form factor	116
B.2 Rotation of a Two-Dimensional Function	118
B.3 Derivation of the transbilayer part of the form factor in the 2G hybrid model	119
B.4 Correction due to refractive index	121

List of Tables

3.1	Some Amino Acids Data	10
3.2	Number of electrons per lipid and volume per lipid.	22
3.3	Some structural parameters for each component. n_i^e is the number of electrons and ρ_i is the average electron density.	22
3.4	Tat basic structural parameters. The notations are the same as in Table 3.3. $x_{\text{Tat}} = \text{Tat}/(\text{Tat}+\text{Lipid})$	22
3.5	Volume results at 37 °C	33
3.6	Fitting Results for DOPC membranes for the THG (Tat in headgroup) model. $z_{\text{PC}} - z_{\text{CG}} = 3.1 \text{ \AA}$ and $z_{\text{CG}} - z_{\text{HC}} = 1.3 \text{ \AA}$ in all fits.	34
3.7	Fitting Results for DOPC:DOPE (3:1) membranes for the THG model. $z_{\text{PC}} - z_{\text{CG}} = 3.1 \text{ \AA}$ and $z_{\text{CG}} - z_{\text{HC}} = 1.3 \text{ \AA}$ in all fits.	37
3.8	(Numbers are wrong) Fitting Results for DOPC:DOPE (1:1) membranes for the THG model. $\Delta z_1 = z_{\text{PC}} - z_{\text{CG}}$ and $\Delta z_2 = z_{\text{CG}} - z_{\text{HC}}$	37
3.9	Fitting Results of the bound THG model for DOPC membranes. $\Delta z_1 = z_{\text{PC}} - z_{\text{CG}}$ and $\Delta z_2 = z_{\text{CG}} - z_{\text{HC}}$	44
3.10	Comparison of the simulated form factors to the experimental form factors.	51
3.11	Summary of simulation results. $\langle D_{\text{PP}} \rangle$, phosphorus-phosphorus distance averaged over all lipids; D_{PP} , Tat-perturbed phosphorus atoms; x , thickness away from Tat; Δt , $\langle D_{\text{PP}}^{\text{DOPC}} \rangle - D_{\text{PP}}$; H_{Tat} , Tat height; R_{Tat} , radius of Tat cylinder; R_2 , radius of the calculated in-plane Tat-perturbed region; R_3 , effective radius of the simulation box.	52
3.12	Summary of weighted average results. The caption is the same as Table 3.11.	52

4.1	Lattice constants for DMPC at $T = 18.0$ °C reported by Wack and Webb [76]. The data collected and analyzed in this thesis are colored blue.	62
4.2	Beam divergence	64
4.3	Energy dispersion	65
4.4	Geometric broadening	71
4.5	Definitions of Z_{CH_2} and Z_{W}	96
4.6	Observed intensity for $h = 1$ to 3 at $D = 57.8$, $\lambda_r = 145$, and $\gamma = 98.2^\circ$. *Unoriented data are from Wack and Webb [76].	99
4.7	Observed intensity for $h = 4$ to 9 at $D = 57.8$, $\lambda_r = 145$, and $\gamma = 98.2^\circ$ (continued from Table 4.6).	100

List of Figures

1.1	Experimental phase diagram of DMPC from Ref. [1].	1
3.1	LAXS of DOPC:DOPE (1:1) with $x_{\text{Tat}} = 0.034$ at 37 °C. White lobes of diffuse scattering intensity have large grey numbers, while lamellar orders and beam are shown to the left of the molybdenum beam attenuator (short, dark rectangle). q_z and q_r are the cylindrical coordinates of the sample q -space, where q_z -axis is along the bilayer normal and q_r -axis is along the in-plane direction. The lamellar repeat spacing was $D = 66.2 \text{ \AA}$	12
3.2	Schematic of an oriented stack of lipid bilayers. Thick green curves represent an instance of thermally fluctuating bilayers. The dashed lines show the thermally averaged positions $z = nD$ of the centers of each bilayer and $u_n(x, y)$ gives the instantaneous deviation from the average. Each bilayer extends in the $\mathbf{r} = (x, y)$ plane.	13
3.3	Expanded view of a fluctuating bilayer. Along the two black solid lines, the electron density profile is identical in an incompressible bilayer. Along the dashed line, the bilayer appears thicker by a factor $1/\cos \alpha$. This apparent thickness variation along the z direction is corrected by the undulation correction.	14
3.4	Schematic of DOPC showing each lipid component. The dash lines show where the lipid is divided into different components. The lipid headgroup is divided into two components, phophate-choline (PC) and carbonyl-glycerol (CG). The hydrocarbon chain region is also divided into two components, methylene+methine (CH_2+CH) and terminal methyl groups (CH_3).	18
3.5	A model electron density profile for DOPC with Tat.	19

3.6 Our simple model to extract the local bilayer thickness from simulation trajectories. Tat is modeled as a cylinder with its height H_{Tat} and radius R_{Tat} . The local thickness is defined as $D'_{\text{phos-phos}}$. The thickness of the unperturbed DOPC bilayer is $D_{\text{phos-phos}}$. Blue highlighted lipids fall within the imaginary cylinder extended from the Tat. Unperturbed lipids are highlighted in green.	27
3.7 Simple model of the lateral decay of the membrane thickness perturbation due to Tat.	29
3.8 Bilayer bending modulus, K_c , vs. Tat mole fraction x_{Tat} . D -spacings for DOPC/Tat mixtures varied from 64 to 68 Å, for DOPC/DOPE/Tat mixtures from 64 to 69 Å, for DOPC/DOPS/Tat (3:1) mixtures from 57 Å to 100 Å (pure DOPS was unbound), and for nuclear mimic/Tat mixtures from unbound (nuclear mimic) to 64 Å. Estimated uncertainty in all values is about ± 2	31
3.9 Form factors of lipid mixtures (arbitrarily scaled and vertically displaced) with increasing Tat mole fractions x_{Tat} indicated on figure legends. Lipid mixtures: A. DOPC B. DOPC/DOPE (3:1) C. DOPC/DOPE (1:1) D. DOPC/DOPS (3:1) E. Nuclear mimic. The entire q_z range is shown in C, while others show partial ranges. Solid vertical lines indicate the q_z values where the form factors equal zero between the lobes of diffuse data.	32
3.10 The best fits to DOPC form factors (left) and the corresponding electron density profiles (right) with $x_{\text{Tat}} = 0, 0.016, 0.034$, and 0.059 (from top to bottom).	35
3.11 The best fits to DOPC:DOPE (3:1) form factors (left) and the corresponding electron density profiles (right) with $x_{\text{Tat}} = 0, 0.016, 0.034$, and 0.059 (from top to bottom).	36
3.12 The best fits to DOPC:DOPE (1:1) form factors (left) and the corresponding electron density profiles (right) with $x_{\text{Tat}} = 0, 0.016, 0.034$, and 0.059 (from top to bottom).	38
3.13 Modeling results for absolute electron density profiles and for the Tat location as a function of distance z along the bilayer normal. A. DOPC B. DOPC:DOPE (3:1), and C. DOPC:DOPE (1:1).	39

3.14 A. Bilayer thickness, D_{PP} ; B. Bilayer thickness, D_{HH} ; C. Area/lipid, A_L ; D. Twice the Tat location, $2z_{\text{Tat}}$: all plotted vs. Tat mole fraction x_{Tat} . Error bars are standard deviations from imposing Tat Gaussian widths, $\sigma_{\text{Tat}} = 2.5, 3.0$ or 3.5 \AA . Inverted blue triangles connected with dotted line are results from MD simulations, averaging the best fits to the X-ray data for each parameter, with standard deviations shown.	41
3.15 χ^2 as a function of z_{Tat} for DOPC, DOPC:DOPE (3:1), and DOPC:DOPE (1:1) (from left to right) with $x_{\text{Tat}} = 0.016, 0.034$, and 0.059 (from top to bottom). $\sigma_{\text{Tat}} = 3.0$. The THG model (black squares) and the THC model (red circles).	42
3.16 χ^2 as a function of z_{Tat} for DOPC with $x_{\text{Tat}} = 0.016, 0.034$, and 0.059 (from top to bottom). $\sigma_{\text{Tat}} = 3.0$. The bound THG model was used.	45
3.17 DPP graph with bound fits	46
3.18 DHH graph with bound fits	46
3.19 AL graph with bound fits	46
3.20 zTat graph with bound fits	46
3.21 MD simulated form factors for DOPC at $A_L = 68 \text{ \AA}^2$ (blue solid line), 70 \AA^2 (red solid line), and 72 \AA^2 (green solid line) compared to the experimental form factor (open circles) scaled vertically to best match the form factor for 70 \AA^2	47
3.22 The simulated, symmetrized electron density profile for DOPC at $A_L = 70 \text{ \AA}^2$ as a function of the distance away from the bilayer center. Each component profile is labeled with its name: PC (phosphate-choline), CG (carbonyl-glycerol), CH ₂ +CH (methylene-methine combination), CH ₃ (terminal methyl). The sum of all the components is labeled as total.	48
3.23 MD simulated form factors for DOPC with $x_{\text{Tat}} = 0.015$ at $A_L = 72 \text{ \AA}^2$ (top) and 74 \AA^2 (bottom), with $z_{\text{Tat}} = 18 \text{ \AA}$ (red solid lines), 16 \AA (green solid lines), and 14 \AA (blue solid lines) compared to the experimental form factor (open circles) scaled vertically to best match the form factor for $z_{\text{Tat}} = 18 \text{ \AA}$	49

3.24 MD simulated form factors for DOPC with $x_{\text{Tat}} = 0.030$ at $A_L = 74 \text{ \AA}^2$ (top) and 76 \AA^2 (bottom), with $z_{\text{Tat}} = 18 \text{ \AA}$ (red solid lines), 16 \AA (green solid lines), and 14 \AA (blue solid lines) compared to the experimental form factor (open circles) scaled vertically to best match the form factor for $z_{\text{Tat}} = 18 \text{ \AA}$	50
3.25 Electron density profiles of guanidinium groups from the four best matched simulations for DOPC with $x_{\text{Tat}} = 0.015$ (one Tat on each leaflet). Tat on the lower and upper leaflets are shown on the left and right plots, respectively.	53
3.26 MD simulated form factors (red solid lines in A and C) of Tat/(DOPC+Tat), $x_{\text{Tat}}=0.030$, with Tat fixed at $z_{\text{Tat}}= 18 \text{ \AA}$ (panel A) and 5 \AA (panel C) from the bilayer center compared to experimental form factors (open circles) scaled vertically to provide the best fit to the simulations. Corresponding snapshots are shown in Panels B and D in which the lipid chains are represented as grey sticks on a white background, Tats are yellow, phosphate groups are red and water is blue.	54
3.27 Location of Tat in DOPC bilayer. Tat is represented as a cylinder, z is the distance from the bilayer center, and R is the in-plane distance from the center of Tat. The average z of the lipid phosphates as a function of R and the arginine guanidiniums are shown in red and blue, respectively.	55
4.1 Lattice structure of the asymmetric ripple phase. Unit cells are shown in dash lines. Center of bilayers are shown by thick, solid lines. Notations in the figure are (a and b : lattice unit vectors), (D : D -spacing along z), ($\lambda_r = \mathbf{b} $: ripple wavelength), (γ : oblique tilt angle), (A : ripple amplitude), (ψ : chain tilt angle with respect to the z direction), and (x_M : projected length of the major arm).	61
4.2 Pictures of an annealing chamber	63
4.3 The horizontal profile of the beam used in the 2013 low resolution study. Each pixel was 0.07113 mm, which gave a CCD angular resolution $\Delta\theta$ of 0.0057° , corresponding to $\Delta q = 0.0011 \text{ \AA}^{-1}$ at the sample to detector distance of 359.7 mm. The beam FWHM = 1.7 pixels, giving $\Delta\theta = 0.010^\circ$ or $\Delta q = 0.0019 \text{ \AA}^{-1}$	66

4.4	The vertical profile of the beam used in the 2013 low resolution study. The beam height = 15 pixels = 1.1 mm.	66
4.5	In-plane geometric broadening due to the sample width w_s and the beam width Δx_{beam} . A top view of the sample (green) on the Si wafer (gray) and the incoming and diffracted X-rays (bounded by red solid lines) are shown. The total in-plane scattering angle for a lipid chain-chain correlation is labeled as 2θ , and the geometric broadening as Δx	68
4.6	The horizontal profile of the beam used in the 2013 high resolution experiment. The CCD angular resolution $\Delta\theta = 0.0092^\circ$ corresponding to $\Delta q = 0.0017 \text{ \AA}^{-1}$, at the sample to detector distance of 220.6 mm. The beam FWHM = 3.7 pixels = 0.26 mm, giving $\Delta\theta = 0.034^\circ$ or $\Delta q = 0.0063 \text{ \AA}^{-1}$	68
4.7	The vertical profile of the beam used in the 2013 high resolution experiment. The beam height = 9 pixels = 0.64 mm.	69
4.8	Geometric broadening in TWAXS	70
4.9	Top and side view of the beam on the sample in TWAXS	71
4.10	Projection of rectangular beam on the detector. Scattered beam appears as a parallelogram on the CCD.	71
4.11	1 second exposure (left) and 60 second exposure (right) of the low angle X-ray scattering from the DMPC ripple phase in gray log scales. The index h is labeled in green. $(3, k)$ reflections are identified in cyan. The shadow cast by 100 μm thick molybdenum attenuator blocking strong $(1, 0)$ and $(2, 0)$ orders in the right image is labeled as attenuator and extends from $q_z = 0 \text{ \AA}^{-1}$ to 0.2 \AA^{-1} . $D = 57.8 \text{ \AA}$, $\lambda_r = 145.0 \text{ \AA}$, and $\gamma = 98.2^\circ$	73

4.12 CCD images of X-ray scattering taken with (left) and without (right) a nominally $25 \mu\text{m}$ thick Mo attenuator. These data were taken at a fixed angle of incidence $\omega = 0.8^\circ$. The sample was an oriented film of DOPC:DOPE (3:1) in the fluid phase at 37°C . The wavelength was 1.175 \AA , the same as the one used for the ripple phase experiment. The same gray scale is used in both images. $100 \text{ pixel} = 0.11 \text{ \AA}^{-1}$ in q . A small dot located about $(p_x, p_z) = (520, 170)$ between the first and second orders is a specular reflection from the substrate. The exposure times were 1 second.	74
4.13 Vertical p_z slices of X-ray images shown in Fig. 4.12 (left). The scattering intensity measured with the attenuator (red solid circles) was multiplied by a factor of 6.9 and compared to the intensity measured without the attenuator (black solid circles, right).	75
4.14 Schematics of the sample holder in the transmission mode. Side (left) and top (right) views are shown. The thickness of the Si wafer = $35 \mu\text{m}$. The thickness of the sample $\approx 10 \mu\text{m}$. The distance between the axis of rotation and sample = 21.1 mm	77
4.15 Circular path followed by the sample as the angle of incidence ω was changed. The sample to detector distance and D -spacing of the sample were measured in the LAXS mode, where $\omega = 1^\circ$. WAXS images were collected at the transmission mode, where $\omega = -45^\circ$. The z position of the sample was slightly higher at the LAXS mode than at the transmission mode, so the sample holder was vertically shifted for different modes.	78
4.16 Picture of the sample holder looking from above. A lead tape was attached to the back of the sample holder to help reduce the background scattering, typically coming from the air gap between the flightpath snout and the mylar window of the chamber.	78
4.17 Experimental reflectivity geometry.	81

4.18 Ewald sphere construction for the ripple phase diffraction in the low angle regime. A ripple $k = 0$ peak is the solid, black circle on the q_z -axis. A ripple $k \neq 0$ ring is the black ring centered about the q_z -axis. The portion of the ring that is inside the Ewald sphere is shown as a red dashed line and the portion of the ring that is outside but behind the Ewald sphere is shown as a black dotted line. The magnitude of the total scattering angle is exaggerated. With a wavelength of 1.175 Å, the magnitude $ \mathbf{k}_{\text{in}} = 5.35 \text{ \AA}^{-1}$. For a $h = 5$ peak, $q_{50}^z = 0.54 \text{ \AA}^{-1}$, one tenth of k_{in} .	83
4.19 Side view of an arc of $k = 0$ peak shown as a thick blue line.	84
4.20 q -space representations of Bragg peaks and Bragg rings for $h = 1$ and 2 and $k = 0, 1$, and 2 in q_{hk}^z planes. The intersection between the Ewald sphere and a Bragg peak/ring is indicated in red. The observed intensity for the $k \neq 0$ orders is proportional to the fraction of the length of red arcs in the circumference. This fraction is equal to one for $k = 0$ reflections. Because the reflections are not in the same q_z plane, the range of q_y integration indicated by the height of the gray rectangle is different for different h orders. For $\gamma \neq 90^\circ$, the range of q_y integration is slightly different for different k reflections with the same h . The values shown are for $D = 58 \text{ \AA}$, $\lambda_r = 145 \text{ \AA}$, $\gamma = 90^\circ$, and $\lambda = 1.175 \text{ \AA}$. The magnitude of curvature of arcs is exaggerated.	85
4.21 The path of X-rays within the sample. The incident angle is ω and the total scattering angle is 2θ . An X-ray with a penetration depth of z is shown. The total thickness of the sample is t .	88
4.22 Absorption factors as a function of $q_z \approx 4\pi\theta/\lambda$. Values at $q_z = 2\pi h/D$ corresponding to $D = 57.8 \text{ \AA}$ are shown as squares. $\mu = 2600 \mu\text{m}$, $t = 10 \mu\text{m}$, and $\lambda = 1.175 \text{ \AA}$.	90
4.23 Contours of a mosaic spread distribution projected on the $\omega\chi$ -plane, where χ is an angle measured from the meridian ($\chi = \pi/2 - \phi$). The distribution function takes a form of Lorentzian centered at $\alpha = 0$. Domains with $\alpha = 0$ are probed at $\omega = \theta_B$ and $\chi = 0$. Integrated intensity of $(1, k)$ reflection is proportional to the green shaded area while that of $(3, k)$ reflection is proportional to the blue shaded area, which is three times larger. The rocking scan ω axis is centered at θ_B .	92

4.24	Mosaic factor given by Eq. (4.37) as a function of $q_z \approx 4\pi\theta/\lambda$	93
4.25	title goes here	95
4.26	NGIWAXS of the DMPC ripple phase for $D = 59.2 \text{ \AA}$ (left) and 60.8 \AA (right). The angle of incidence ω was 0.2° . The black regions around the edge of each image are the q -space that was not probed. The distorted, non rectangular shape of the probed q -space signifies non-linear relation between the CCD space and sample q -space.	102
4.27	Enlarged view of the right image in Fig. 4.26. To show smaller features around the peak, a different contrast is used.	103
4.28	q_r swaths, each averaged over 0.02 \AA^{-1} . The center q_z value of a swatch is shown in the figure legends.	104
A.1	Two dimensional view of mosaic spread (left) and notations used in this section (right). The stacking direction of an ideal domain is n and that of a tilted domain n' . The deviation of n' from n denoted as α quantifies the degree of misorientation of a domain. The x , y , and z -axes are the sample coordinates.	108
A.2	Example of a two dimensional sample consisting of an ideal and tilted domains. $\mathbf{q} = (q_x, q_z)$ is the sample q -space and $\mathbf{q}' = (q'_x, q'_z)$ is the domain q -space. The two q -spaces are related by a rotation of α about the y -axis, which is into the page.	109
A.3	Notations used in this section. The arc originating from the Z -axis is the mosaic arc due to the mosaic spread distribution.	112
A.4	Rocking scan trace in q -space.	113

Chapter 4

Ripple Phase

When the temperature is reduced from the fluid phase, the ripple phase is observed in bilayers consisting of DMPC and DPPC lipids. This chapter discusses X-ray scattering experiments on the ripple phase formed by dimyristolphosphatydylcholine (DMPC) bilayers.

4.1 Introduction

(At some point, do some literature search and write up this section) The ripple phase has been a fascinating thermodynamic phase to many physicists and physical chemists since its discovery. It was originally observed in calorimetry study for alkanes by sturevant. Although this phase has never been reported to occur in a biologically relevant situation, it provides an interesting opportunity to study fundamental lipid interactions and their influence on the bilayer shape. (Let's find some recent papers and see if anyone says anything about biological relevance)

In the first structural study of this phase by Tardieu *et al.*, the X-ray diffraction pattern from DLPC was phased by a pattern recognition technique and the electron density map was calculated. It was shown that the structure corresponds to a 2D oblique unit cell shown in Fig. 4.1. The calculated electron density map showed that DLPC bilayers are height modulated and have a smooth, asymmetric shape. The ripple wavelength λ_r was reported to be 85.3 Å, the lamellar periodicity D 55.3 Å, and the oblique angle γ 110°. The electron density map reported the ripple amplitude $A = 15$ Å in DLPC.

Various experiments have indicated the existence of two types of ripple phases: the

stable asymmetric and the metastable symmetric phase. In the asymmetric phase, a plane of reflection perpendicular to the ripple wave vector is absent. The metastable symmetric phase has been seen in DPPC bilayers, but not in DMPC.

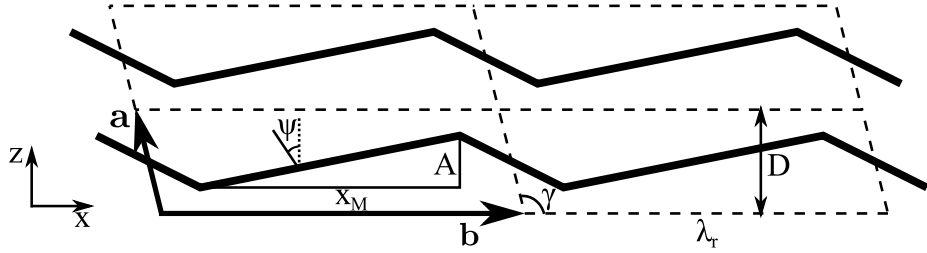


Figure 4.1: Lattice structure of the asymmetric ripple phase. Unit cells are shown in dash lines. Center of bilayers are shown by thick, solid lines. Notations in the figure are (**a** and **b**: lattice unit vectors), (D : D -spacing along z), ($\lambda_r = |\mathbf{b}|$: ripple wavelength), (γ : oblique tilt angle), (A : ripple amplitude), (ψ : chain tilt angle with respect to the z direction), and (x_M : projected length of the major arm).

The equilibrium structure of the ripple phase has been extensively studied by X-ray diffraction [1, 74–79], neutron diffraction [80, 81], AFM [], freeze fracture electron microscopy [82], and freeze fracture scanning tunneling microscopy [] techniques. In the scanning tunneling microscopy experiment [83], the three-dimensional contours of the ripple phase $P_{\beta'}$ of dimyristoylphosphatidylcholine (DMPC) were imaged, and a ripple wavelength of 130 Å and an amplitude of 45 Å were reported.

multilayer vs LUV. Any LUV paper report on ripple?

From X-ray data of the DMPC ripple of unoriented samples, Wack and Webb [76] argued that the ripples have a sawtooth shape, but were unable to phase the observed pattern. Their X-ray form factor data were later phased by employing a modeling and fitting technique by Sun *et al.* [78], and the electron density map was calculated, which indicated that the ripples indeed have a sawtooth shape. The map also showed that the major arm is about twice as long as the minor arm. The bilayer thickness was found to be larger than that of the minor arm. The value of the bilayer thickness in the major arm was comparable to the thickness of DMPC bilayers in the gel phase whereas the thickness of the minor arm was comparable to that in the fluid phase.

A structural investigation by X-ray diffraction of the ripple phase of oriented dipalmitoylphosphatidylcholine (DPPC) samples indicated that hydrocarbon chains are packed in a hexagonal lattice with chains tilted in the plane perpendicular to the ripple wave vector [84]. In that study, the oblique angle γ was found to be 90°.

Katsaras and Raghnathan papers

Several MD (molecular dynamics) simulations have been carried out, indicating various lipid packing. de Vrie *et al.* has suggested interdigitated chain in the minor side [85].

Some theory papers

D (Å)	λ_r (Å)	γ (deg)
55.0	159.4	99.0
57.0	140.8	97.6
57.3	151.6	97.8
57.4	148.4	97.6
57.5	144.1	97.8
57.5	141.9	98.0
58.0	140.1	98.2
57.8	145.0	98.2
58.0	141.7	98.4
59.8	129.6	97.3
60.6	130.1	97.0
61.5	130.8	96.5
62.4	122.0	95.9
63.9	123.1	94.9
64.9	120.3	92.3

Table 4.1: Lattice constants for DMPC at $T = 18.0$ °C reported by Wack and Webb [76]. The data collected and analyzed in this thesis are colored blue.

4.2 Materials and Methods

4.2.1 Sample Preparation

DMPC was purchased from Avanti Polar Lipids. Oriented thin films were deposited on clean silicon wafers with a chloroform:methanol 2:1 (volume ratio) mixture following the rock and roll procedure [86]. See also Sec. 3.2.1. In 2011 and 2012 synchrotron experiments, the samples were created and annealed more than a week in advance and stored in a refrigerator. The quality of these samples measured by their mosaic spread was found to worsen over time after the samples were annealed. Therefore, to attempt better quality, the samples were annealed for only about 12 hours just before the X-ray experiment. Figure 4.2 shows a picture of the annealing chamber. Annealing is promoted both by hydration and by elevated temperature. To achieve gentle but efficient hydration of a sample, filter papers were installed that exposed a larger surface for evaporation. The temperature was set to 60 °C. It must be emphasized that the annealing chamber should equilibrate in an annealing oven set to 60 °C, prior to putting a sample in the chamber. When a sample was put in the chamber sitting at a room temperature and then the system was placed inside the oven, warmer water vapor inside the chamber condensed on the cooler sample, causing so called flooding of oriented sample. A small drop of water on an oriented film is detrimental for the orientation quality because the entropy-driven formation of unilamellar vesicles causes oriented bilayers to peel off one by one.

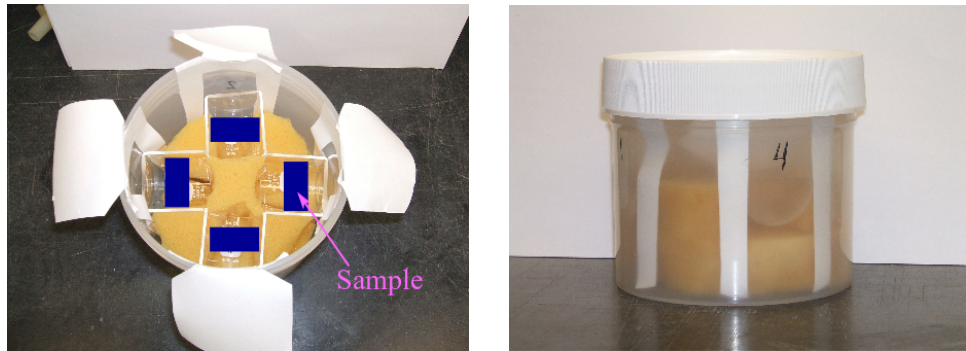


Figure 4.2: Picture of an annealing chamber.

The sample for the grazing incident wide angle study was prepared in the same way as for low angle study. In order to minimize the geometric broadening, the sample was trimmed to 1 mm in width along the beam direction.

The sample for transmission study was deposited on a thin, 35 micron, silicon wafer, and oriented following the rock and roll procedure [86]. Because the wafer was very fragile, attaching the sample to a sticky thing was impossible. Instead, the sample was attached to a plastic cap on a small vial with a small amount of heat sink compound at a corner of the wafer. The wafer was stable enough for rocking.

4.2.2 Instrumental Resolution

The X-ray scattering experiments were carried out at the Cornell High Energy Synchrotron Source (CHESS) G1 station in three different runs (2011, 2012, and 2013). The low angle X-ray scattering (LAXS) data analyzed in this thesis were collected in 2013. The near grazing incidence wide angle X-ray scattering (NGIWAXS) data were also collected in the 2013 run, but with smaller energy dispersion than in the LAXS experiment. The transmission wide angle X-ray scattering (TWAXS) data were collected in the 2011 run. The ripple phase experiment in the 2012 run was not successful due to low sample quality. The instrumental resolution in these X-ray experiments depended on the beam divergence, energy dispersion, and geometric broadening.

Divergence

The beam divergence quantifies an angular spread of the incoming X-ray beam. We estimated the beam divergence by measuring the horizontal and vertical beam widths at two known sample-to-detector S distances with difference ΔS . The beam widths were larger at the further distance, which indicated that the beam was divergent. We calculated the divergence as $\text{div} = \Delta B / \Delta S$, where ΔB is the difference in beam widths at different S distances. Table 4.2 summarizes beam divergence.

year	type of experiment	horizontal (rad.)	vertical (rad.)
2013	LAXS	4.2×10^{-5}	1.6×10^{-4}
2013	NGIWAXS	4.2×10^{-5}	1.6×10^{-4}
2011	TWAXS	2.5×10^{-5}	5×10^{-5}

Table 4.2: Beam divergence

Energy dispersion

A W/B₄C multilayer monochromator with energy bandwidth $\Delta E/E$ of 1.3% was used in the LAXS and TWAXS experiments. The energy of the X-ray beam was 10.55 keV, corresponding to a wavelength λ of 1.175 Å, in the LAXS experiment. To achieve a higher instrumental resolution than that for the LAXS experiment, a (111) silicon monochromator was used for the NGIWAXS experiment, which gave $\Delta E/E$ of 0.01%. Due to the geometry of the G1 station, the Si monochromator was placed in the G1 hutch, in series with the multilayer monochromator. Table 4.3 summarizes energy dispersion.

year	type of experiment	$\Delta E/E$ (%)	E (keV)	λ (Å)
2013	LAXS	1.5	10.55	1.175
2013	NGIWAXS	0.01	10.55	1.175
2011	TWAXS	1.5	10.54	1.176

Table 4.3: Energy dispersion

Geometric Broadening

The beam footprint on the sample has a finite size and this causes geometric broadening of diffraction peaks on the CCD detector.

In the LAXS experiment, the geometric broadening in the horizontal x direction is simply the horizontal beam width for $k = 0$ peaks with minor additional broadening for $k \neq 0$ peaks. Geometric broadening in the vertical z direction is due to different heights of the sample along the y direction of the beam at non zero angle of incidence ω . It is given approximately by $w_s \tan \theta$, where w_s is the sample width along the y direction and θ is the scattering angle. The beam shape, measured through a semi-transparent 200 µm thick molybdenum (Mo) beam stop, is shown in Fig. 4.3 and 4.4. The horizontal beam width was 1.7 pixels (0.12 mm). The vertical beam width was approximately 1 mm, tall enough to cover the entire sample if the sample was tilted between 0° and 11.5°. The sample was rocked during X-ray exposure between -1.6° and 7° in order to observe many diffraction peaks in one data collection and keep all the sample in the beam.

In the NGIWAXS experiment, the horizontal geometric broadening was due to the sample width along the beam direction and the horizontal beam width. From the

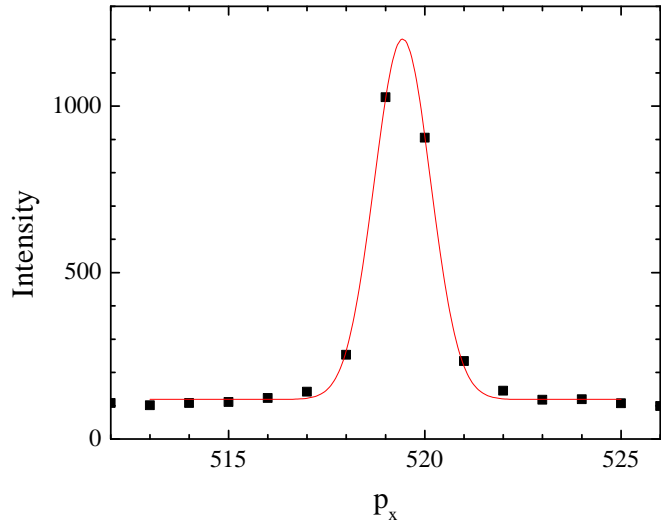


Figure 4.3: The horizontal profile of the beam used in the 2013 low resolution study. Each pixel was 0.07113 mm, which gave a CCD angular resolution $\Delta\theta$ of 0.0057°, corresponding to $\Delta q = 0.0011 \text{ \AA}^{-1}$ at the sample to detector distance of 359.7 mm. The beam FWHM = 1.7 pixels, giving $\Delta\theta = 0.010^\circ$ or $\Delta q = 0.0019 \text{ \AA}^{-1}$.

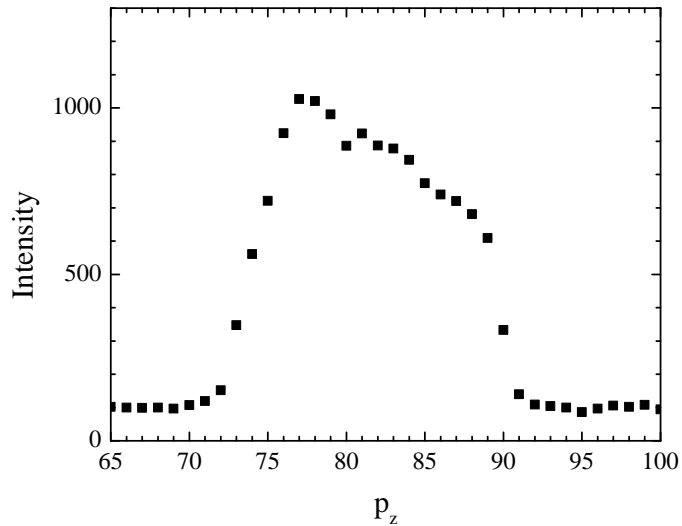


Figure 4.4: The vertical profile of the beam used in the 2013 low resolution study. The beam height = 15 pixels = 1.1 mm.

geometry of the experiment shown in Fig. 4.5, the geometric broadening Δx can be estimated, assuming simple additivity,

$$\Delta x = \Delta x_{\text{beam}} + w_s \tan(2\theta),$$

where θ is the in-plane scattering angle. The total scattering angle 2θ for the ripple WAXS was approximately 16° . To minimize the contribution to Δx from the sample, the sample was trimmed to $w_s = 1$ mm along the beam direction. This width was chosen because (1) I could not trim more without a more sophisticated device than a simple razor blade, (2) a very narrow sample would be a weak scattering body, and (3) disordering effect from the sample edge might become too significant to ignore. Given the above reasons and due to limited availability of synchrotron beam time, I considered a 1 mm width to be reasonable. The horizontal beam width was 4 pixels (0.28 mm) as shown in Fig. 4.6. With these experimental parameters, the resolution was estimated to be $\Delta x = 0.57$ mm = 8 pixels, which would be the unresolved width of an intrinsically infinitely sharp wide angle peak. **Comment and refer to the gel phase data shown in the result section of NGIWAXS.** The sample to detector distance were 220.6 mm, measured using silver behenate. Then, the minimum peak width measured in q -space would be $\Delta q \approx 0.014 \text{ \AA}^{-1}$. The vertical geometric broadening was negligible because the sample width w_s was narrow and scattering of interest occurred at small q_z .

In the TWAXS experiment, geometric broadening in both x and z directions was non-negligible. To calculate the broadening, let us assume that the beam has a rectangular cross section with its height Y_b and width X_b as shown in Figure 4.8. When the sample is tilted by ω , X-rays emerging from the top edge of the sample travel extra distance compared to the distance that X-rays from the bottom edge of the sample travel. This, then, leads to distortion of the scattered beam; namely, the scattered beam will appear on the CCD screen as a parallelogram as shown in Figure 4.8. Figure 4.9 shows the top- and sideview of the projection of the beam on the sample. From simple geometry, it can be shown that $a = Y_b / \tan \omega$, $b = aX/(2S)$, $c = aZ/(2S) + Y_B/2$, and $B = \tan^{-1}(Z/S)$. Since $H = 2c$ and $W = 2b$, H and W in

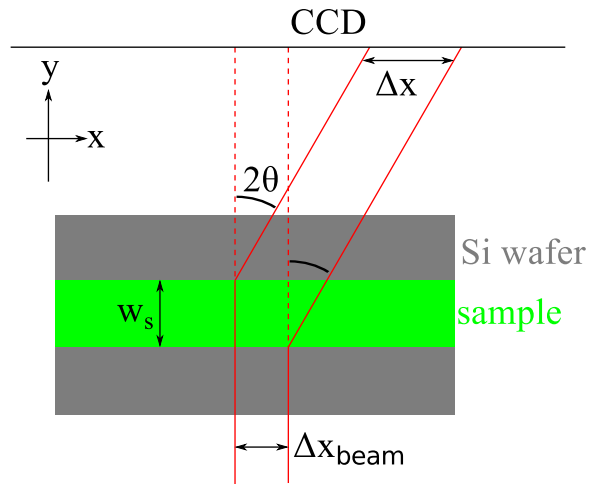


Figure 4.5: In-plane geometric broadening due to the sample width w_s and the beam width Δx_{beam} . A top view of the sample (green) on the Si wafer (gray) and the incoming and diffracted X-rays (bounded by red solid lines) are shown. The total in-plane scattering angle for a lipid chain-chain correlation is labeled as 2θ , and the geometric broadening as Δx .

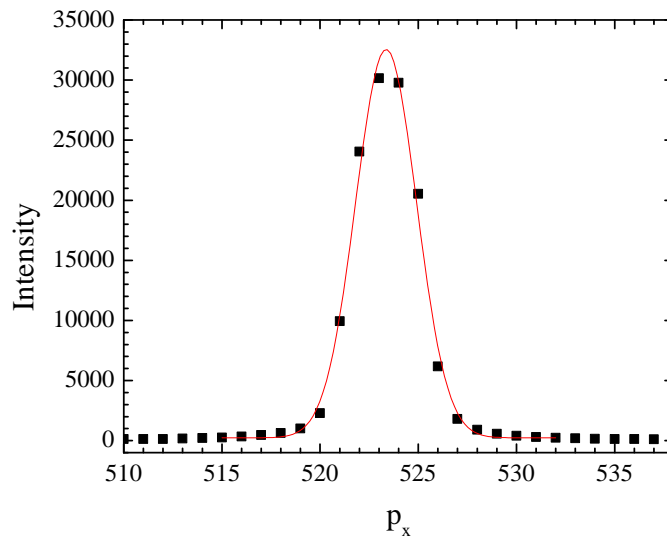


Figure 4.6: The horizontal profile of the beam used in the 2013 high resolution experiment. The CCD angular resolution $\Delta\theta = 0.0092^\circ$ corresponding to $\Delta q = 0.0017 \text{ \AA}^{-1}$, at the sample to detector distance of 220.6 mm. The beam FWHM = 3.7 pixels = 0.26 mm, giving $\Delta\theta = 0.034^\circ$ or $\Delta q = 0.0063 \text{ \AA}^{-1}$.

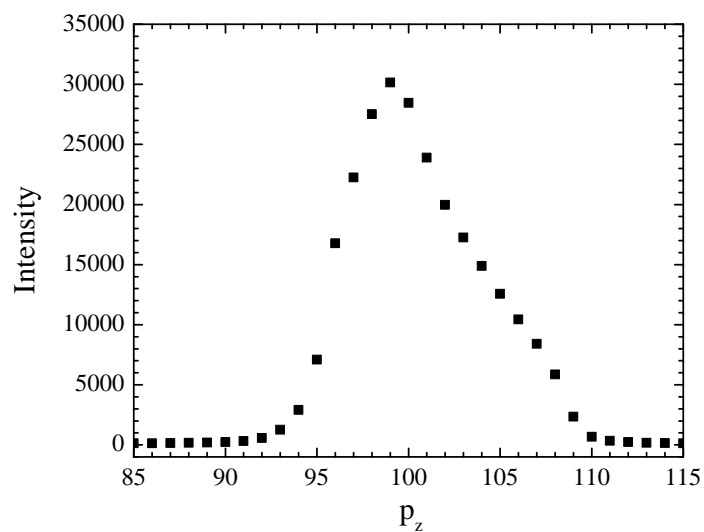


Figure 4.7: The vertical profile of the beam used in the 2013 high resolution experiment. The beam height = 9 pixels = 0.64 mm.

Figure 4.10 are given by

$$H = Y_b \left(1 + \frac{Z}{S \tan \omega} \right) \quad (4.1)$$

$$W = Y_b \frac{X}{S \tan \omega}. \quad (4.2)$$

The sample to detector distance S was 158.6 mm, giving an angular CCD resolution of $0.013^\circ/\text{pixel}$, or $0.0024 \text{ \AA}^{-1}/\text{pixel}$. The observed wide angle peak was at $(X, Z) = (44.0 \text{ mm}, 15.5 \text{ mm})$. The beam width and height were both $0.2 \text{ mm} = 2.8 \text{ pixels}$. With this setup, $W = 0.7 \text{ pixels}$ and $H = 3.1 \text{ pixels}$. Therefore, the distorted shape of the diffraction peak was negligible. Table 4.4 summarizes geometric broadening for our experiments.

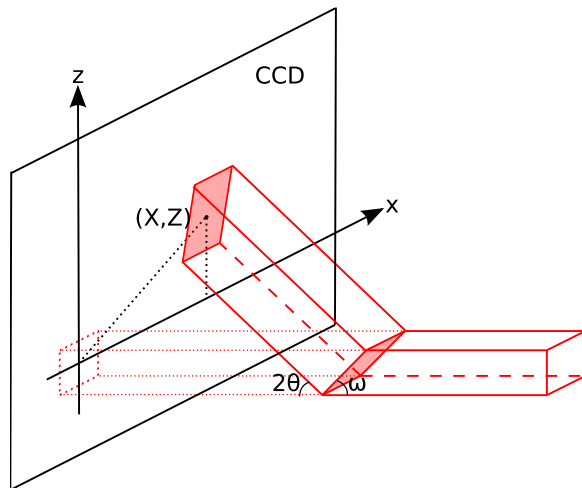


Figure 4.8: Geometric broadening in TWAXS. The cross section of the incoming X-ray with the sample and the CCD detector are both shaded in red. The sample is tilted by ω . The red dots show the transmitted beam. The incoming beam is rectangular but upon scattering appears as a parallelogram on the CCD.

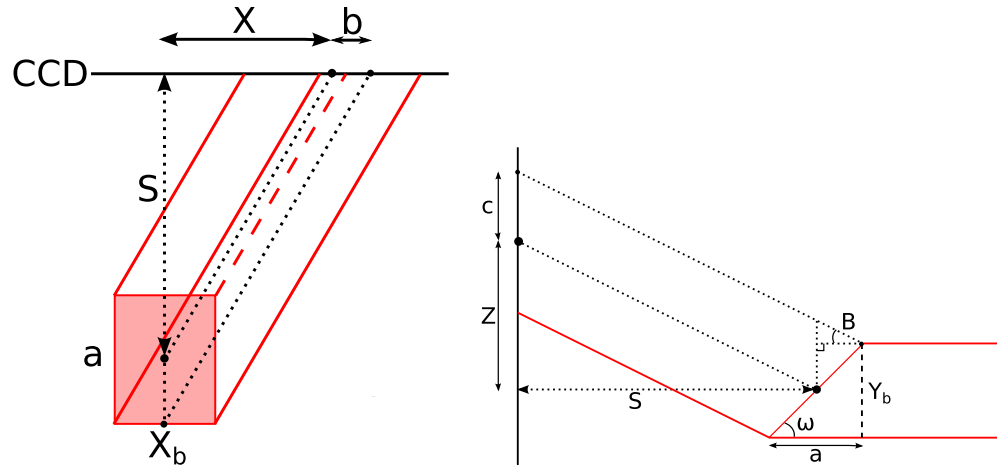


Figure 4.9: Top and side view of the beam on the sample in TWAXS. The cross section of the incoming X-ray with the sample is shaded in red. X_b and Y_b are the beam width and height, respectively. S is the sample to detector distance. (X, Z) is a position of the center of the scattered beam on the detector with respect to the center of the transmitted beam as shown in Figure 4.8.

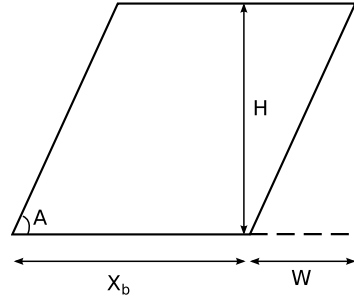


Figure 4.10: Projection of rectangular beam on the detector. Scattered beam appears as a parallelogram on the CCD.

type of experiment	horizontal (pixels)	horizontal (\AA^{-1})	vertical (pixels)	vertical (\AA^{-1})
LAXS	1.7	0.0019	$6.6q_z$	$0.0072q_z$
NGIWAXS	8	0.014		
TWAXS	2.8	0.0067	3.1	0.0074

Table 4.4: Geometric broadening

4.2.3 Low Angle X-ray Scattering Experiment

The X-ray beam for the low angle X-ray scattering (LAXS) experiment was set up by the station scientist, Dr. Arthur Woll. The sample to detector distance was 359.7 mm, measured by indexing silver behenate Bragg peaks. The D-spacing of silver behenate is known to be 58.367 Å.

Occasionally, sheets of molybdenum (Mo), each nominally 25 μm were used to attenuate the incoming beam. These sheets were installed by Dr. Arthur Woll in the upstream of the sample chamber. The attenuation length μ of 10.55 keV X-ray in Mo is 13.74 μm [87]. For a 25 μm thick Mo attenuator, the attenuation factor is calculated to be $[\exp(-25/13.74)]^{-1} = 6.2$. The exact attenuation factor was determined by comparing X-ray images collected with and without the attenuator, shown in Fig. 4.12 and 4.13. The attenuation factor of the nominally 25 μm thick Mo was found to be 6.9 for the wavelength used (1.175 Å).

Sheets of Mo were also used as a beam stop downstream of the sample, just outside the hydration chamber, to attenuate the beam and strong orders. 100 and 200 μm were used to attenuate strong orders and 225 μm to attenuate the beam. To avoid saturation of CCD pixels by the very intense beam, the beam stop was always set to block the beam.

A few Bragg peaks in the low angle X-ray scattering of the ripple phase were very strong, leading to saturation of CCD pixels for data collection with a long exposure time. In order to probe a wide range of q -space, three images were taken: 1) a short, one second exposure with a nominally 25 micron molybdenum attenuator installed in the upstream of the sample to reduce the intensity of the incoming X-ray beam, 2) one second exposure without the beam attenuator, and 3) 60 second exposure with a beam stop blocking the very intense (1,0) and (2,0) peaks. See Fig. 4.11. Then, the integrated intensity of (1,0) peak was measured from the first image. This value was multiplied by 6.9 to account for the beam attenuation and by 60 to scale with the exposure time. The intensity of (2,0) and (2,-1) were measured from the second image, also multiplied by 60 to account for the shorter exposure time. The intensity of the rest of the observed peaks were measured from the third image.

The integrated intensity of each peak was obtained using the Nagle lab tview software developed by Dr. Yufeng Liu [39] by putting a box around a peak and summing up the intensity in those pixels that fall inside the box. The background scattering was estimated by measuring the intensity in pixels near the peak but not

containing any peak tail. The choice of box size was made according to the width of each peak. Because of mosaic spread in the sample, the peaks were wider for higher orders. Consequently, the box was made wider for higher orders. The box size was chosen so that approximately 80% of the peak intensity was counted toward the integrated intensity.

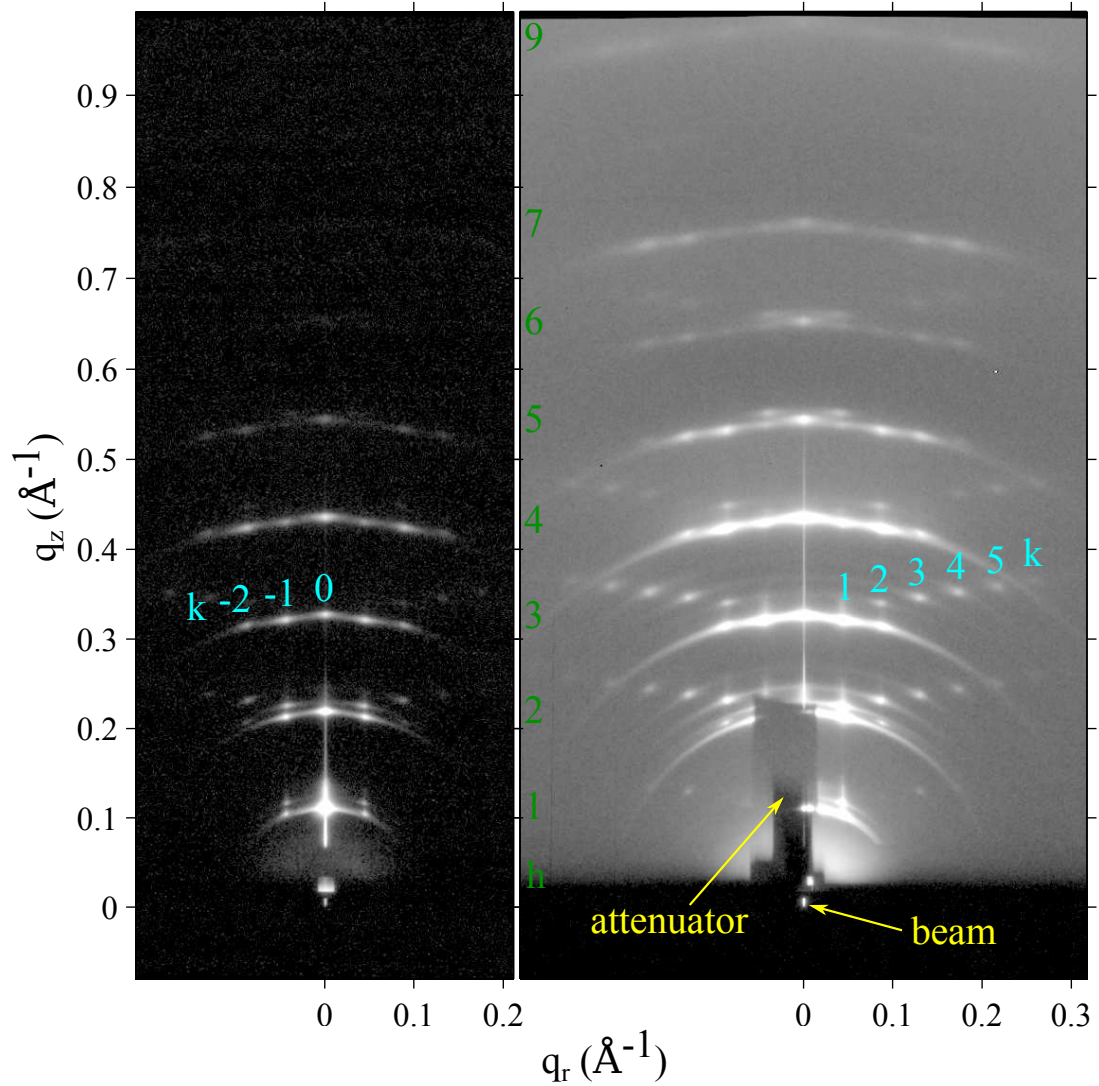


Figure 4.11: 1 second exposure (left) and 60 second exposure (right) of the low angle X-ray scattering from the DMPC ripple phase in gray log scales. The index h is labeled in green. $(3, k)$ reflections are identified in cyan. The shadow cast by 100 μm thick molybdenum attenuator blocking strong $(1,0)$ and $(2,0)$ orders in the right image is labeled as attenuator and extends from $q_z = 0 \text{ \AA}^{-1}$ to 0.2 \AA^{-1} . $D = 57.8 \text{ \AA}$, $\lambda_r = 145.0 \text{ \AA}$, and $\gamma = 98.2^\circ$.

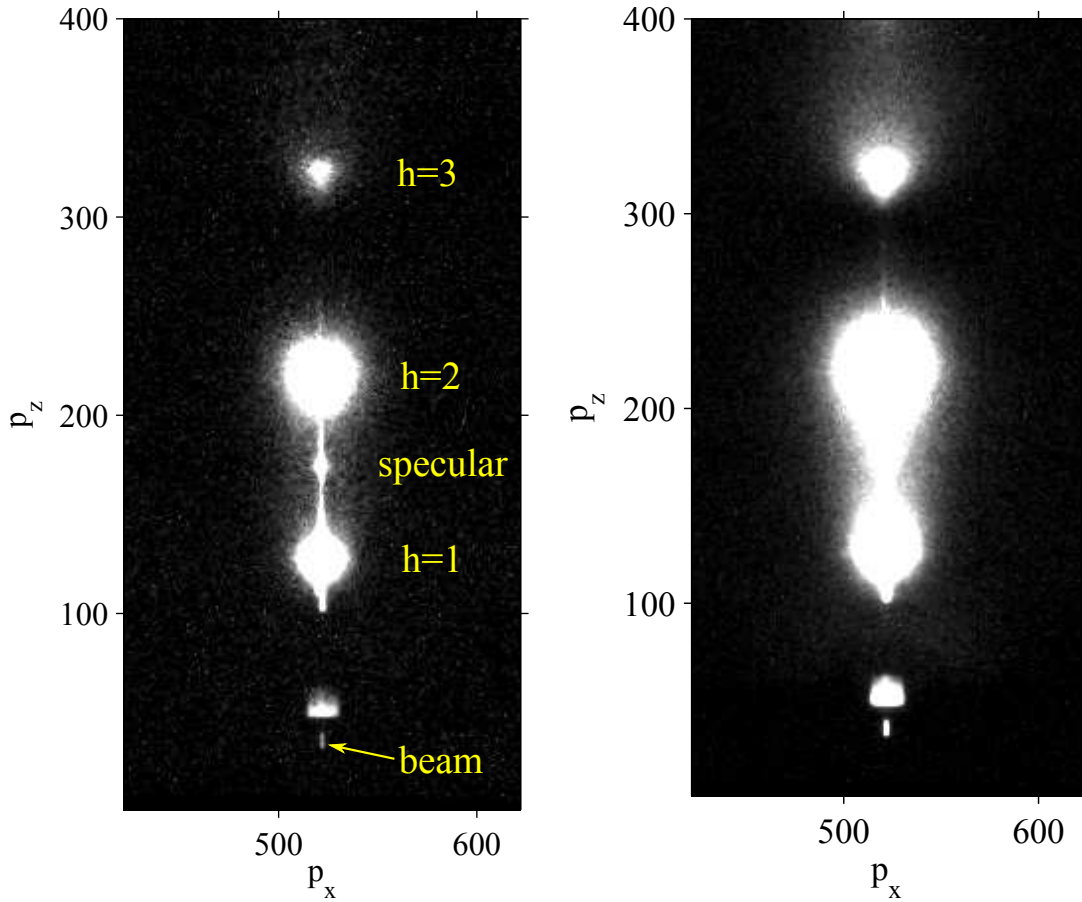


Figure 4.12: CCD images of X-ray scattering taken with (left) and without (right) a nominally $25 \mu\text{m}$ thick Mo attenuator. These data were taken at a fixed angle of incidence $\omega = 0.8^\circ$. The sample was an oriented film of DOPC:DOPE (3:1) in the fluid phase at 37°C . The wavelength was 1.175\AA , the same as the one used for the ripple phase experiment. The same gray scale is used in both images. $100 \text{ pixel} = 0.11 \text{\AA}^{-1}$ in q . A small dot located about $(p_x, p_z) = (520, 170)$ between the first and second orders is a specular reflection from the substrate. The exposure times were 1 second.

4.2.4 Near Grazing Incidence Wide Angle X-ray Scattering Experiment

The high resolution wide angle X-ray scattering (WAXS) experiment was also carried out at the G1 station. The instrument was set up by the G1 station scientist, Author Woll, and the assistant scientist, Dr. Robin Baur. Wide angle X-ray scattering was collected at an incident angle of 0.2° . The total external reflection from an air-lipid interface occurs approximately at 0.1° and 0.17° for air-silicon interface, so 0.2° is not

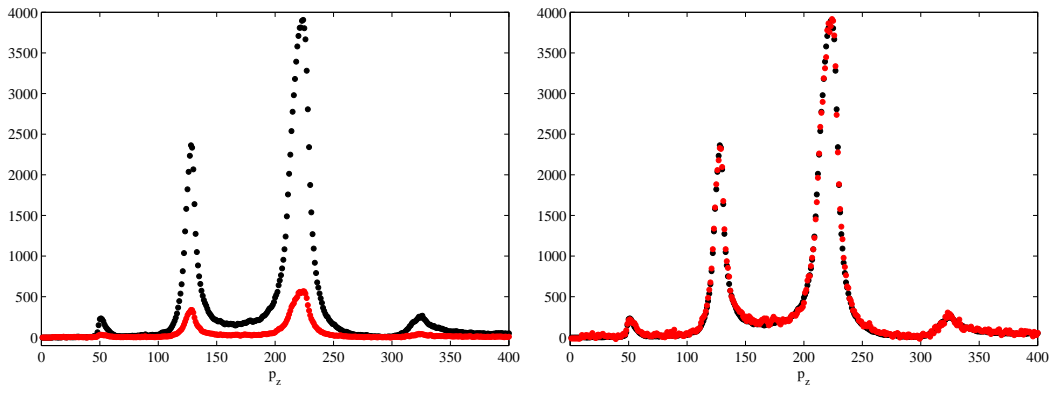


Figure 4.13: Vertical p_z slices of X-ray images shown in Fig. 4.12 (left). The scattering intensity measured with the attenuator (red solid circles) was multiplied by a factor of 6.9 and compared to the intensity measured without the attenuator (black solid circles, right).

quite grazing incidence. Grazing incidence usually implies that the incident angle is less than the critical angle for a total external reflection. Therefore, 0.2° is called near grazing incidence (NGI) in this thesis. The background scattering was collected at -0.2° . Subtraction of the negative angle data from the positive angle data resulted in a clean sample scattering image.

4.2.5 Transmission Wide Angle X-ray Scattering Experiment

The transmission wide angle X-ray scattering (TWAXS) experiment was also carried out at the G1 station. The incident angle ω was set to -45° for transmission data collection (see Fig. 4.14). A $35\ \mu\text{m}$ thick silicon substrate absorbs 10.5 keV X-ray by only 20% [87], so most of the incoming X-rays penetrated the thin substrate. To measure the D-spacing of the sample, ω was set to 1° .

Unfortunately, the axis of the rotation motor did not coincide with the sample axis, so the sample to detector distance varied as ω was varied. To accurately measure the sample to detector distance, low angle scattering from a silver behenate (AgBe) sample was collected at a fixed ω . Due to large mosaic spread of the AgBe sample, many orders were visible. While the relative intensity of each order was inaccurate, the positions of peaks were the same as those observed with a rotating sample. The sample to detector distance was measured to be 174.7 mm at $\omega = 0^\circ$. From the sample holder geometry shown in Fig. 4.15, the sample to detector distance was estimated to be 158.6 mm at $\omega = 45^\circ$. A picture of the sample holder is shown in Fig. 4.16.

To level the sample, the sample was first leveled coarsely by watching the sample scattering. When ω was negative, much of the incoming beam was absorbed by the flat substrate, yielding weak sample scattering. When ω became positive, sample scattering was strong. With this procedure, we leveled the sample with an uncertainty of $\pm 0.2^\circ$. We then measured the beam intensity at various sample heights as a function of ω . The sample was level when the beam intensity had the narrowest dip as the sample was moved vertically through the beam.

Background scattering was collected by replacing the sample with a bare wafer. The bare wafer was not placed exactly at the same location as the sample, which gave slightly different background scattering. This only affected the background subtraction near the beam. The wide angle scattering was not affected by this inexact placement of the bare wafer.

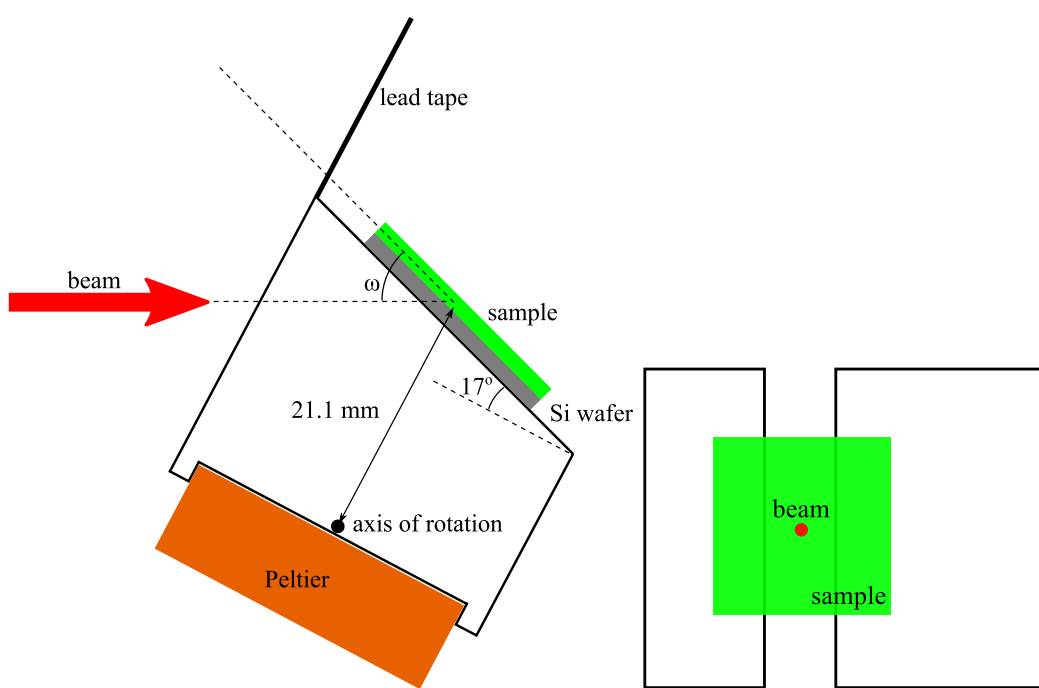


Figure 4.14: Schematics of the sample holder in the transmission mode. Side (left) and top (right) views are shown. The thickness of the Si wafer = $35 \mu\text{m}$. The thickness of the sample $\approx 10 \mu\text{m}$. The distance between the axis of rotation and sample = 21.1 mm.

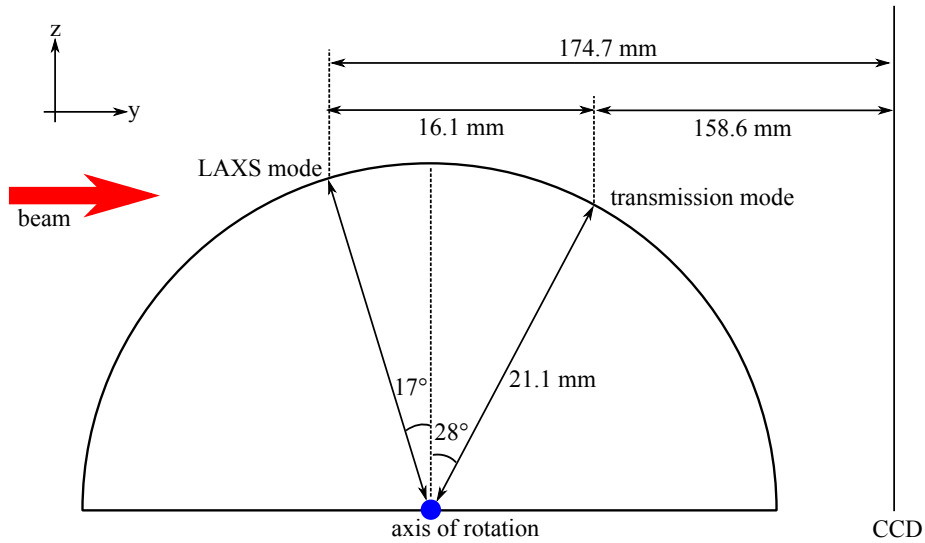


Figure 4.15: Circular path followed by the sample as the angle of incidence ω was changed. The sample to detector distance and D -spacing of the sample were measured in the LAXS mode, where $\omega = 1^\circ$. WAXS images were collected at the transmission mode, where $\omega = -45^\circ$. The z position of the sample was slightly higher at the LAXS mode than at the transmission mode, so the sample holder was vertically shifted for different modes.

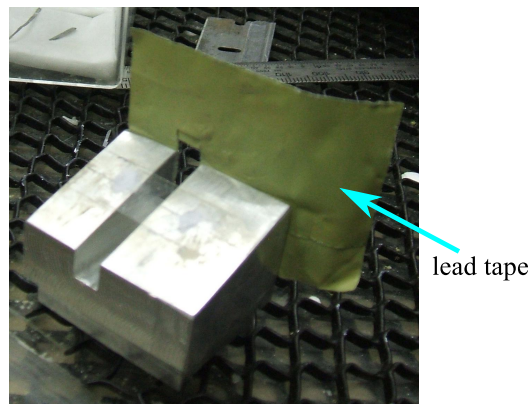


Figure 4.16: Picture of the sample holder looking from above. A lead tape was attached to the back of the sample holder to help reduce the background scattering, typically coming from the air gap between the flightpath snout and the mylar window of the chamber.

4.3 LAXS: analysis

4.3.1 Lattice Structure

The unit cell vectors for the two-dimensional oblique lattice shown in Fig. 4.1 can be expressed as

$$\mathbf{a} = \frac{D}{\tan \gamma} \hat{\mathbf{x}} + D \hat{\mathbf{z}} \quad (4.3)$$

and

$$\mathbf{b} = \lambda_r \hat{\mathbf{x}}. \quad (4.4)$$

The corresponding reciprocal lattice unit cell vectors are

$$\mathbf{A} = \frac{2\pi}{D} \hat{\mathbf{z}} \quad (4.5)$$

and

$$\mathbf{B} = \frac{2\pi}{\lambda_r} \hat{\mathbf{x}} - \frac{2\pi}{\lambda_r \tan \gamma} \hat{\mathbf{z}}. \quad (4.6)$$

The reciprocal lattice vector, \mathbf{q}_{hk} for the Bragg peak with Miller indices (h, k) is

$$\mathbf{q}_{hk} = h\mathbf{A} + k\mathbf{B}, \quad (4.7)$$

so its Cartesian components are

$$\mathbf{q}_{hk} \cdot \hat{\mathbf{x}} = q_{hk}^x = \frac{2\pi k}{\lambda_r} \equiv q_k^x \quad (4.8)$$

$$\mathbf{q}_{hk} \cdot \hat{\mathbf{y}} = q_{hk}^y = 0 \quad (4.9)$$

$$\mathbf{q}_{hk} \cdot \hat{\mathbf{z}} = q_{hk}^z = \frac{2\pi h}{D} - \frac{2\pi k}{\lambda_r \tan \gamma}. \quad (4.10)$$

Our sample consists of many ripple domains with a uniform distribution of in-plane directions of the ripple wave vector, \mathbf{b} in Fig. 4.1. In this case, q_{hk}^x and q_{hk}^y are combined to give $q_{hk}^r = 2\pi k / \lambda_r$.

4.3.2 Sample q-space

The incoming and outgoing wavevectors of the x-ray beam in Fig. 4.17 are given by

$$\mathbf{k}_{\text{in}} = \frac{2\pi}{\lambda} \hat{\mathbf{y}}, \quad \mathbf{k}_{\text{out}} = \frac{2\pi}{\lambda} (\sin 2\theta \cos \phi \hat{\mathbf{x}} + \cos 2\theta \hat{\mathbf{y}} + \sin 2\theta \sin \phi \hat{\mathbf{z}}), \quad (4.11)$$

where λ is the wavelength of x-ray, 2θ is the total scattering angle, and ϕ is the angle measured from the equator on the detector. The scattering vector (also called momentum transfer vector) is the difference between \mathbf{k}_{in} and \mathbf{k}_{out} ,

$$\begin{aligned} \mathbf{q} &= \mathbf{k}_{\text{out}} - \mathbf{k}_{\text{in}} \\ &= q (\cos \theta \cos \phi \hat{\mathbf{x}} - \sin \theta \hat{\mathbf{y}} + \cos \theta \sin \phi \hat{\mathbf{z}}), \end{aligned} \quad (4.12)$$

where $q = 4\pi \sin \theta / \lambda$ is the magnitude of the scattering vector. When the sample is rotated by ω about the lab x-axis in the clockwise direction as shown in Fig. 4.17, the sample q -space also rotates and are given by

$$\hat{\mathbf{e}}_{\mathbf{x}} = \hat{\mathbf{x}}, \quad \hat{\mathbf{e}}_{\mathbf{y}} = \cos \omega \hat{\mathbf{y}} + \sin \omega \hat{\mathbf{z}}, \quad \hat{\mathbf{e}}_{\mathbf{z}} = -\sin \omega \hat{\mathbf{y}} + \cos \omega \hat{\mathbf{z}}. \quad (4.13)$$

From Eq. (4.12) and (4.13), we find Cartesian components of the sample q -space to be

$$\begin{aligned} q_x &= \mathbf{q} \cdot \hat{\mathbf{e}}_{\mathbf{x}} = q \cos \theta \cos \phi, \\ q_y &= \mathbf{q} \cdot \hat{\mathbf{e}}_{\mathbf{y}} = q (-\sin \theta \cos \omega + \cos \theta \sin \phi \sin \omega), \\ q_z &= \mathbf{q} \cdot \hat{\mathbf{e}}_{\mathbf{z}} = q (\sin \theta \sin \omega + \cos \theta \sin \phi \cos \omega). \end{aligned} \quad (4.14)$$

The position, (X, Z) , of a CCD pixel is measured with respect to the beam and given by

$$X = S \tan 2\theta \cos \phi, \quad Z = S \tan 2\theta \sin \phi, \quad (4.15)$$

where S is the distance between the sample and detector.

From a model for the electron density of a lipid bilayer, one calculates the X-ray scattering intensity pattern, $I(\mathbf{q})$. Then, Eq. (4.14) and (4.15) relate $I(\mathbf{q})$ to the experimentally measured intensity pattern, $I(X, Z)$. It is important to remember that a given pixel position, (X, Z) , corresponds to a triplet (q_x, q_y, q_z) . Fully exploring the sample q -space requires changing ω for a fixed wavelength, which was achieved

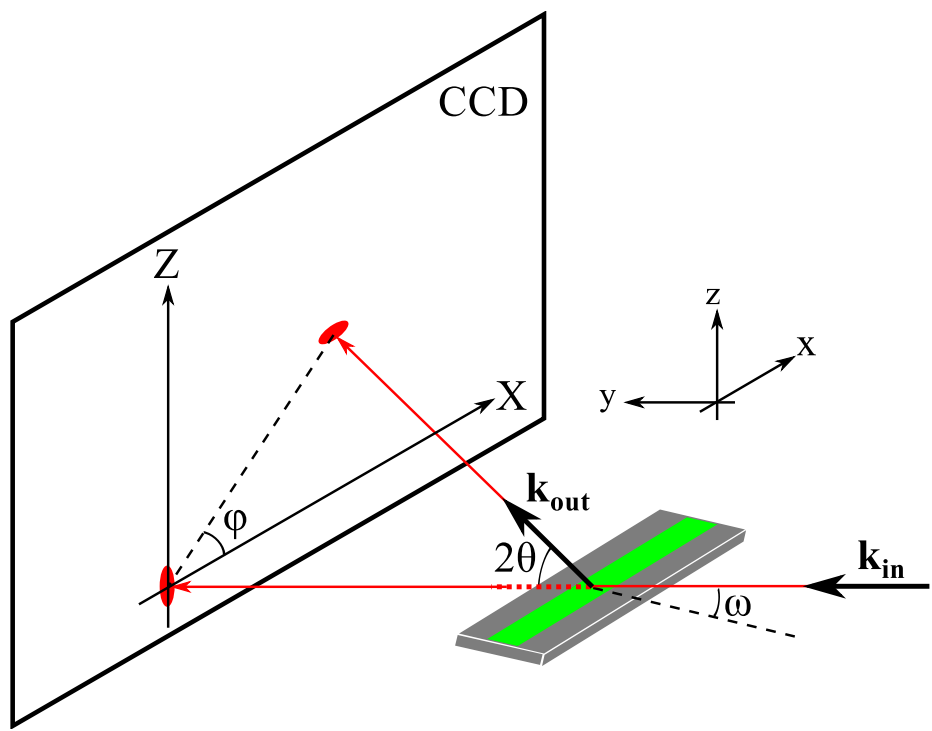


Figure 4.17: Experimental reflectivity geometry.

by continuously rotating the sample with a motor. In the ripple phase, because our sample has in-plane rotational symmetry, the ripple side peaks ($h, k \neq 0$) make up Bragg rings while the main peaks ($h, k = 0$) are still delta function like (see Fig. 4.18) in q -space. In order for the main peak to be observed, ω must be equal to θ_B , but the side peaks are observed at any ω . Those side peaks get slightly smeared due to integration over q_y .

For low angle x-ray scattering (LAXS), it is convenient to linearize the above equations in terms of θ and ω . In the small angle approximation, $\sin \phi \approx Z/(2S\theta)$ and $\cos \phi \approx X/(2S\theta)$, and

$$\begin{aligned} q_x &\approx \frac{4\pi\theta \cos \phi}{\lambda} \approx kX/S \\ q_y &\approx q_z \omega - \frac{4\pi\theta^2}{\lambda} \approx q_z \omega - \frac{\lambda q_z^2}{4\pi} \\ q_z &\approx \frac{4\pi\theta \sin \phi}{\lambda} \approx kZ/S, \end{aligned} \quad (4.16)$$

with $k = 2\pi/\lambda$. For wide angle X-ray scattering, the exact relations given by Eq. (4.14) are necessary. Especially in the transmission experiment, where ω is large, an observed X-ray pattern appears nontrivial and becomes almost impossible to analyze without the use of Eq. (4.14). The transmission experiment is discussed in Sec.4.9.

4.3.3 Lorentz Correction

Our sample has in-plane rotational symmetry about the z -axis. Ignoring mosaic spread to which we will come back later, this means that the sample consists of many domains with differing ripple directions, all domains being parallel to the substrate. In sample q -space, ripple ($h, k \neq 0$) side peaks are represented as rings centered at the meridian, or q_z -axis, while ($h, k = 0$) main peaks are still points on the meridian (see Fig. 4.18). Then, for an arbitrary incident angle ω , ($h, 0$) peaks are not observed while side peaks are observed for a range of ω as will now be explained.

In order to capture all (h, k) peaks in one X-ray exposure, the sample was continuously rotated over a range of $\omega, \Delta\omega$, about the x -axis. As a result of this rotation, the ($h, 0$) main peaks become arcs that subtend an angle $\Delta\omega$, as shown in Fig. 4.19, with its length equal to $\Delta\omega q_{h0}$. The detector records the intersections of these arcs

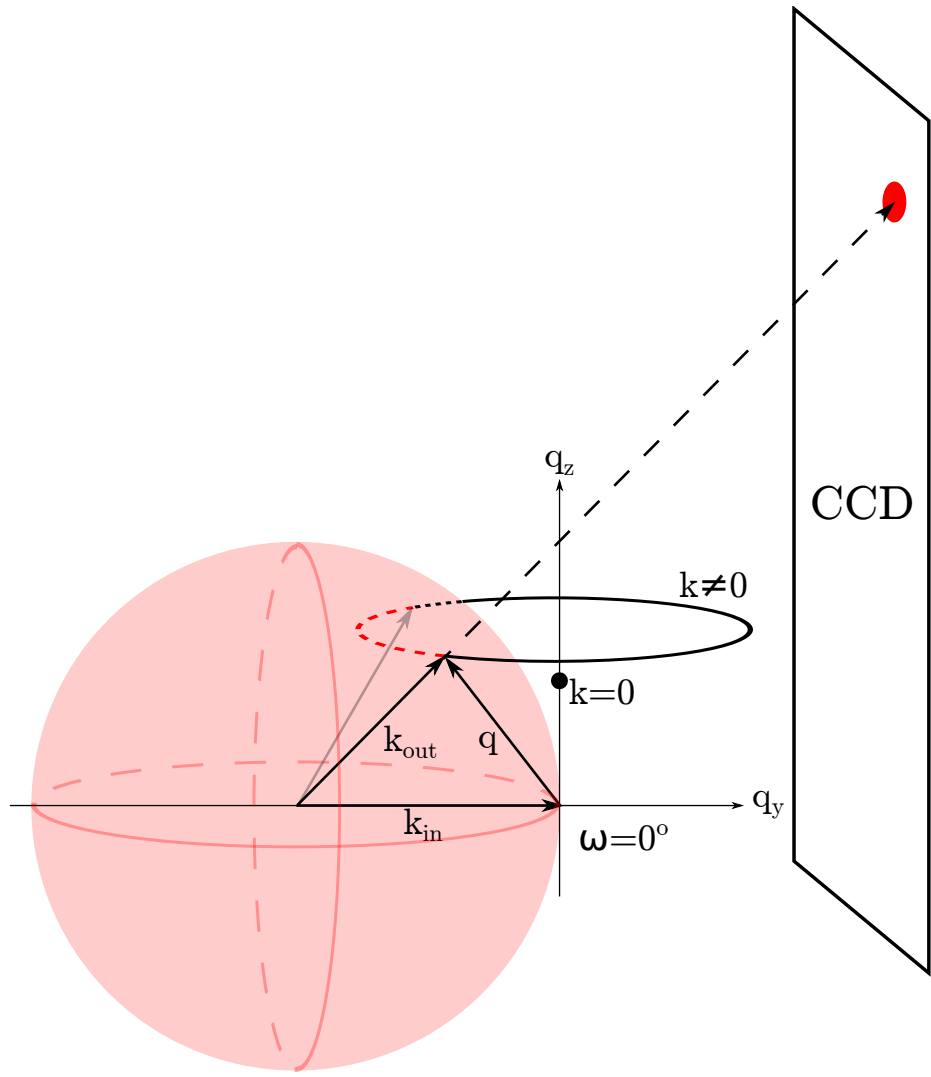


Figure 4.18: Ewald sphere construction for the ripple phase diffraction in the low angle regime. A ripple $k = 0$ peak is the solid, black circle on the q_z -axis. A ripple $k \neq 0$ ring is the black ring centered about the q_z -axis. The portion of the ring that is inside the Ewald sphere is shown as a red dashed line and the portion of the ring that is outside but behind the Ewald sphere is shown as a black dotted line. The magnitude of the total scattering angle is exaggerated. With a wavelength of 1.175 \AA , the magnitude $|k_{in}| = 5.35 \text{ \AA}^{-1}$. For a $h = 5$ peak, $q_{50}^z = 0.54 \text{ \AA}^{-1}$, one tenth of k_{in} .

with the Ewald sphere, so the intrinsic scattering intensity of the $(h, k = 0)$ reflections is the product of the observed intensity, I_{hk}^{obs} with the arc length, that is,

$$I_{h0} = \Delta\omega q_{h0}^z I_{h0}^{\text{obs}}. \quad (4.17)$$

This is the usual Lorentz correction for lamellar orders.

Now, we consider relative intensity of side peaks for a given order h . As described earlier, $(h, k \neq 0)$ side peaks are represented as rings whose radius is q_{hk}^r in the sample q -space. Because only the domains with the right ripple direction can satisfy the Bragg's condition at a given fixed angle ω , the intrinsic scattering intensity in this ring is reduced by a factor of $2\pi q_{hk}^r$ compared to the $(h, 0)$ reflections. This reduction of intensity can be nicely visualized by the Ewald sphere construction shown in Fig. 4.18, which shows that the entire rings are not intersected by the Ewald sphere at a fixed angle. Then, the intrinsic scattering intensity in a ring is

$$I_{hk \neq 0} \propto 2\pi q_{hk}^r I_{hk}^{\text{obs}}. \quad (4.18)$$

During an X-ray exposure, the sample q -space rotates and the rings are intersected by the Ewald sphere at all our experimental incident angles ω . However, as Fig. 4.20 shows, only small parts of the rings are actually intersected with the Ewald sphere. To obtain the full expression for $(h, k \neq 0)$ reflections, we now turn to a more rigorous calculation.

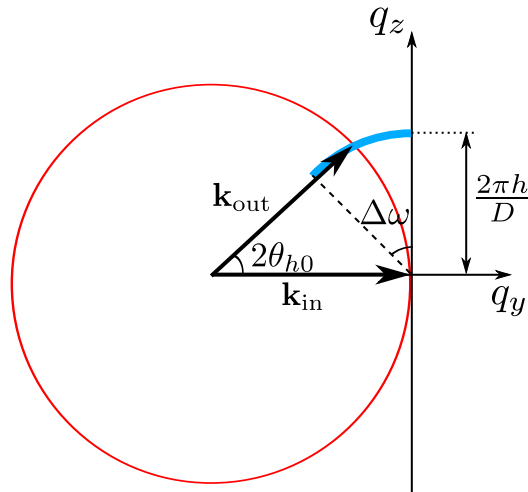


Figure 4.19: Side view of an arc of $k = 0$ peak shown as a thick blue line.

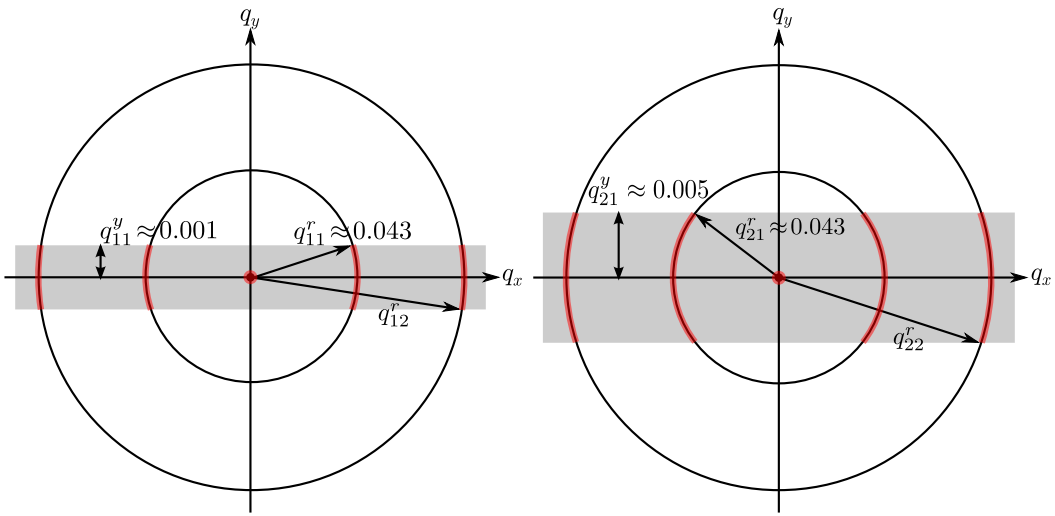


Figure 4.20: q -space representations of Bragg peaks and Bragg rings for $h = 1$ and 2 and $k = 0, 1$, and 2 in q_{hk}^z planes. The intersection between the Ewald sphere and a Bragg peak/ring is indicated in red. The observed intensity for the $k \neq 0$ orders is proportional to the fraction of the length of red arcs in the circumference. This fraction is equal to one for $k = 0$ reflections. Because the reflections are not in the same q_z plane, the range of q_y integration indicated by the height of the gray rectangle is different for different h orders. For $\gamma \neq 90^\circ$, the range of q_y integration is slightly different for different k reflections with the same h . The values shown are for $D = 58$ Å, $\lambda_r = 145$ Å, $\gamma = 90^\circ$, and $\lambda = 1.175$ Å. The magnitude of curvature of arcs is exaggerated.

Mathematically, the rotation is equivalent to an integration over ω . In low angle X-ray scattering, q_z is nearly constant at a given pixel as ω is changed, which can be seen from Eq. (4.16). As Eq. (4.16) shows, ω dependence appears only through q_y , so rotating the sample is realized by integrating over q_y ; formally, we write $d\omega = dq_y/q_z$. To derive the integration limits on q_y , let us consider two cases: (1) When $\omega \leq 0$, the incoming X-ray beam is blocked by the back of the substrate. This sets the lower limit of ω to 0. Plugging $\omega = 0$ in Eq. 4.16), we find the lower limit of the q_y integration to be $-\lambda q_z^2/(4\pi)$. (2) When $\omega \geq 2\theta$, the substrate blocks the outgoing X-ray, so the maximum $\omega = 2\theta$. Within the small angle approximation, $q_z \approx 4\pi\theta/\lambda$. Then, the maximum ω can be expressed as $\lambda q_z/(2\pi)$. Plugging this expression for ω in Eq. (4.16), we find the upper limit of the q_y integration to be $\lambda q_z^2/(4\pi)$. Also integrating over the detector pixels X and Z to obtain integrated intensity, we write the observed intensity as

$$\begin{aligned} I_{hk}^{\text{obs}} &\propto \int dX \int dZ \int d\omega I_{hk} \\ &\propto \int dq_x \int dq_z \int_{-\frac{\lambda q_z^2}{4\pi}}^{\frac{\lambda q_z^2}{4\pi}} \frac{dq_y}{q_z} I_{hk}(\mathbf{q}), \end{aligned} \quad (4.19)$$

where $1/q_z$ factor in q_y integration is the usual Lorentz polarization factor in the small angle approximation.

For a crystalline sample with in-plane rotational symmetry, the structure factor of a ripple Bragg peak is

$$S_{hk}(\mathbf{q}) = S_{hk}(q_r, q_z) = \frac{1}{2\pi q_r} \delta(q_r - q_{hk}^r) \delta(q_z - q_{hk}^z), \quad (4.20)$$

where $q_{hk}^r = 2\pi|k|/\lambda_r$. Thus, the scattering pattern in the ripple phase is a collection of Bragg rings for $k \neq 0$ centered at the meridian and the Bragg peaks for $k = 0$ located along the meridian. The scattering intensity is $I(\mathbf{q}) = |F(\mathbf{q})|^2 S(\mathbf{q})$, where $F(\mathbf{q})$ is the form factor. After the q_z integration, the observed, integrated intensity of (h, k) peak is proportional to

$$I_{hk}^{\text{obs}} \propto \frac{|F_{hk}|^2}{q_{hk}^z} \int dq_x \int_{-q_{hk}^{y0}}^{q_{hk}^{y0}} dq_y \frac{\delta(q_r - q_{hk}^r)}{2\pi q_r}, \quad (4.21)$$

where $q_{hk}^{y0} = \lambda(q_{hk}^z)^2/(4\pi)$. For side peaks ($k \neq 0$), we have

$$\begin{aligned} \int dq_x \int_{-q_{hk}^{y0}}^{q_{hk}^{y0}} dq_y \frac{\delta(q_r - q_{hk}^r)}{2\pi q_r} &\approx \int_{-q_{hk}^{y0}/q_{hk}^r}^{q_{hk}^{y0}/q_{hk}^r} d\phi \int dq_r q_r \frac{\delta(q_r - q_{hk}^r)}{2\pi q_r} \\ &= \frac{q_{hk}^{y0}}{\pi q_{hk}^r}. \end{aligned} \quad (4.22)$$

For main peaks ($k = 0$), we have

$$\begin{aligned} \int dq_x \int_{-q_{hk}^{y0}}^{q_{hk}^{y0}} dq_y \frac{\delta(q_r - q_{hk}^r)}{2\pi q_r} &= \int_0^{2\pi} d\phi \int dq_r q_r \frac{\delta(q_r - q_{hk}^r)}{2\pi q_r} \\ &= 1 \end{aligned} \quad (4.23)$$

Using Eq. (4.21 – 4.23), we write the observed integrated intensity as

$$I_{h0}^{\text{obs}} \propto \frac{|F_{h0}|^2}{q_{h0}^z} \quad (4.24)$$

$$I_{hk}^{\text{obs}} \propto \frac{|F_{hk}|^2}{q_{hk}^z} \frac{q_{hk}^{y0}}{\pi q_{hk}^r} = |F_{hk}|^2 \frac{\lambda q_{hk}^z}{2\pi} \frac{1}{2\pi q_{hk}^r} = |F_{hk}|^2 \frac{2\theta_{hk}}{2\pi q_{hk}^r}, \quad (4.25)$$

where $2\theta_{hk} = \lambda q_{hk}^z/(2\pi)$ is the incident angle at which the outgoing X-ray for the peak (h, k) is blocked by the substrate. Eq. (4.24) and (4.25) relate the form factor calculated from a model to the experimentally observed intensity, and are partially equivalent to Eq. (4.17) and (4.18).

In non-linear least squares fitting procedure, we fitted the observed integrated intensity to the calculated intensity from a bilayer model using these Lorentz corrections. This is because we can determine experimental uncertainties on observed intensity rather than the Lorentz-corrected form factors. We avoid propagating the uncertainties by fitting a model to observed intensity.

4.3.4 Absorption Correction for LAXS

In this section, we derive the absorption correction for an oriented sample. The calculation involves an explicit integration over the incident angle, ω , which is necessitated by the sample rotation during an X-ray exposure. The procedure is to write down an absorption factor, $A(\omega, \theta)$, for a given scattering angle at a given incident angle,

and then integrate over ω . We ignore q_x dependence because the X-ray path inside the sample is nearly within the y - z plane for low angle scattering. The correction for wide angle scattering is described in a later section.

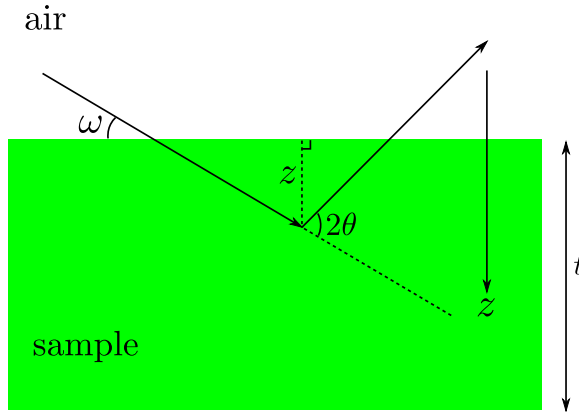


Figure 4.21: The path of X-rays within the sample. The incident angle is ω and the total scattering angle is 2θ . An X-ray with a penetration depth of z is shown. The total thickness of the sample is t .

Assume that all the X-rays enter the sample from the top surface. The total scattering angle is given by 2θ (see Fig. 4.21). Let the z -axis point downward. At the top surface (air-sample interface), $z = 0$. For X-rays that travel to z and then scatter, the total path length within the sample is

$$L_{\text{tot}}(z, \omega, \theta) = \frac{z}{\sin \omega} + \frac{z}{\sin(2\theta - \omega)} = z g(\omega, \theta), \quad (4.26)$$

where $g(\omega, \theta) = (\sin \omega)^{-1} + (\sin(2\theta - \omega))^{-1}$. For each ray, the intensity is attenuated by the sample absorption. If non-attenuated intensity is equal to I_0 , then the attenuated intensity is

$$I(z, \omega, \theta) = I_0 \exp\left(-\frac{L_{\text{tot}}}{\mu}\right), \quad (4.27)$$

where μ is the absorption length of an X-ray. μ is 2.6 mm for 10.5 keV [87]. The observed intensity of scattering from a sample fixed at an angle ω is equal to the

integration of Eq. (4.27) over the total thickness of the sample and given by

$$\begin{aligned} I_{\text{obs}}(\omega, \theta) &= \int_0^t dz I(z, \omega, \theta) = I_0 \int_0^t dz \exp\left(-\frac{g(\omega, \theta)}{\mu} z\right) \\ &= I_0 \mu \frac{1 - \exp\left(-\frac{t}{\mu} g(\omega, \theta)\right)}{g(\omega, \theta)}. \end{aligned} \quad (4.28)$$

Defining the absorption factor at a fixed angle to be $A(\omega, \theta)$, the observed intensity can also be written as

$$I_{\text{obs}}(\omega, \theta) = A(\omega, \theta) t I_0, \quad (4.29)$$

where $t I_0$ is the intensity we would observe for non-absorbed X-rays. Equating Eq. (4.28) and (4.29), we get

$$A(\omega, \theta) = \frac{\mu}{t} \frac{1 - \exp\left(-\frac{t}{\mu} g(\omega, \theta)\right)}{g(\omega, \theta)}. \quad (4.30)$$

If μ is taken to infinity (no absorption), $A(\omega, \theta)$ goes to 1 as expected. The absorption factor A_{h0} for the $k = 0$ peaks is given by $A(\omega = \theta = \theta_B)$, plotted in Fig. 4.22. As shown, this factor is about 20 % for $h = 1$ peak with respect to $h = 4$, so it is not negligible.

For $k \neq 0$ side peaks, an integration over the incident angle ω is necessary because these peaks are observable at all our experimental incident angles as described in section 4.3.3. The total observed intensity from a rotating sample is simply

$$I_{\text{total}}(\theta) = \int_0^{2\theta} d\omega I_{\text{obs}}(\omega, \theta). \quad (4.31)$$

The upper integration limit is equal to 2θ because the substrate completely blocks the scattered X-rays above this angle as discussed in section 4.3.3. The total non-attenuated intensity is equal to $2\theta t I_0$. We, then, define the absorption factor $A(\theta)$ to be the ratio of the total observed intensity to the total non-attenuated intensity,

$$A(\theta) \equiv \frac{I_{\text{total}}(\theta)}{2\theta t I_0}. \quad (4.32)$$

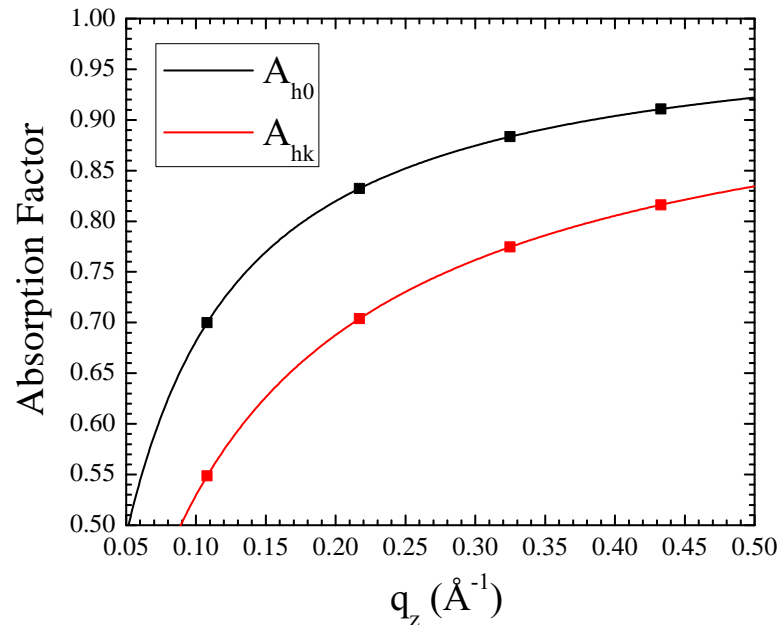


Figure 4.22: Absorption factors as a function of $q_z \approx 4\pi\theta/\lambda$. Values at $q_z = 2\pi h/D$ corresponding to $D = 57.8 \text{ \AA}$ are shown as squares. $\mu = 2600 \mu\text{m}$, $t = 10 \mu\text{m}$, and $\lambda = 1.175 \text{ \AA}$.

Using Eq. (4.30) and (4.31) in (4.32), we arrive at the final absorption factor

$$A(\theta) = \frac{1}{2\theta} \int_0^{2\theta} d\omega A(\omega, \theta) = \frac{\mu}{2\theta t} \int_0^{2\theta} d\omega \frac{1 - \exp\left(-\frac{t}{\mu}g(\omega, \theta)\right)}{g(\omega, \theta)}. \quad (4.33)$$

$A_{hk} = A(\theta)$ is plotted in Fig. 4.22. The absorption correction $A_c(\theta)$ is the inverse of Eq. (4.33).

4.3.5 Correction due to mosaic spread

Integrated intensity needs to be corrected for mosaic spread. During an X-ray exposure, the sample was continuously rotated. Due to this rotation, each pixel integrates intensity over a range of incident angles ω . As described in appendix A.2.2, a mosaic spread distribution can be probed by changing ω , so rotating the sample is essentially equivalent to integrating a mosaic spread distribution. Because the range of the distribution probed is given by $\omega = 2\theta_{hk}$ where θ_{hk} is the Bragg angle for the (h, k) reflection, this range is larger for higher h orders. This effect is illustrated in Fig. 4.23.

We limit χ to go from -1.4° to 1.4° . The effect of cutoff on χ is not very important because most of observed intensity was included in integration boxes. In contrast, cutoff on ω due to substrate blocking the scattering is important, especially for lower h orders.

We take the distribution to be Lorentzian, which has been experimentally observed,

$$P(\alpha) = \frac{N}{\alpha^2 + \alpha_M^2}, \quad (4.34)$$

where N is a normalization constant and α_M is the HWHM of the distribution. N satisfies

$$N \approx \frac{1}{2\pi} \left(\int_0^{\frac{\pi}{2}} d\alpha \frac{\alpha}{\alpha^2 + \alpha_M^2} \right)^{-1}. \quad (4.35)$$

We then consider a two dimensional contour map on a $\omega\chi$ plane. Intensity for a reflection with a Bragg angle of θ_B is given by

$$I = \int_{-\theta_B}^{\theta_B} d\omega \int_{-\chi_0}^{\chi_0} d\chi P(\alpha) = \int_{-\theta_B}^{\theta_B} d\omega \int_{-\chi_0}^{\chi_0} d\chi \frac{N}{(\omega - \theta_B)^2 + \chi^2 + \alpha_M^2} \quad (4.36)$$

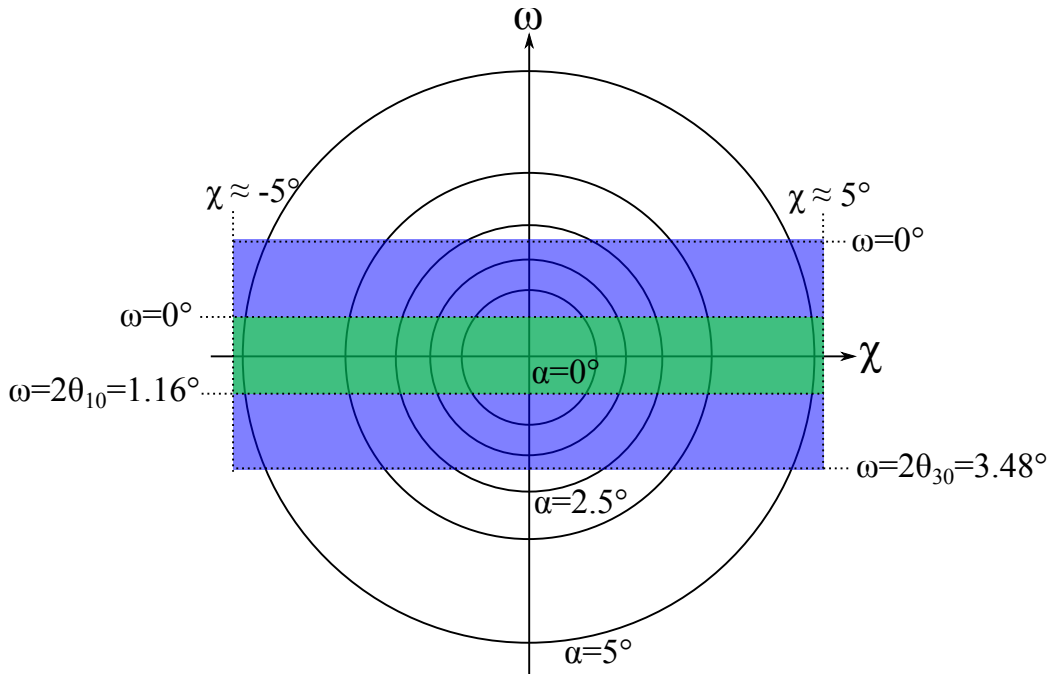


Figure 4.23: Contours of a mosaic spread distribution projected on the $\omega\chi$ -plane, where χ is an angle measured from the meridian ($\chi = \pi/2 - \phi$). The distribution function takes a form of Lorentzian centered at $\alpha = 0$. Domains with $\alpha = 0$ are probed at $\omega = \theta_B$ and $\chi = 0$. Integrated intensity of $(1, k)$ reflection is proportional to the green shaded area while that of $(3, k)$ reflection is proportional to the blue shaded area, which is three times larger. The rocking scan ω axis is centered at θ_B .

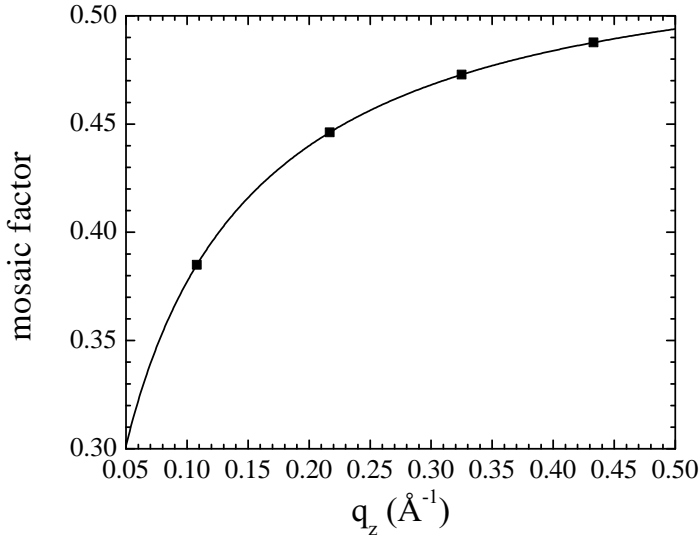


Figure 4.24: Mosaic factor given by Eq. (4.37) as a function of $q_z \approx 4\pi\theta/\lambda$. Values at $q_z = 2\pi h/D$ corresponding to $D = 57.8 \text{ \AA}$ are shown as squares. $\alpha_M = 0.05^\circ$ and $\chi_0=1.4^\circ$.

After the integration over χ , Eq. (4.36) is

$$I = 4N \int_0^{\theta_B} \frac{d\omega}{\sqrt{\omega^2 + \alpha_M^2}} \arctan\left(\frac{\chi_0}{\sqrt{\omega^2 + \alpha_M^2}}\right). \quad (4.37)$$

Eq. (4.37) is plotted in Fig. 4.24.

4.4 LAXS: model

4.4.1 Contour Part of the Form Factor

As in Ref. [78], we take the ripple profile to have a sawtooth profile. Its amplitude is A and the projection of the major arm on the ripple direction is x_M as shown in Fig. 4.1. Then, we write the ripple profile as

$$u(x) = \begin{cases} -\frac{A}{\lambda_r - x_0} \left(x + \frac{\lambda_r}{2} \right) & \text{for } -\frac{\lambda_r}{2} \leq x < -\frac{x_0}{2}, \\ \frac{A}{x_0} x & \text{for } -\frac{x_0}{2} \leq x \leq \frac{x_0}{2}, \\ -\frac{A}{\lambda_r - x_0} \left(x - \frac{\lambda_r}{2} \right) & \text{for } \frac{x_0}{2} < x \leq \frac{\lambda_r}{2}. \end{cases} \quad (4.38)$$

The ripple profile has inversion symmetry, so that the resulting form factor is real. A and x_M are fitting parameters that depend on the integrated intensity of each peak while D , λ_r , and γ are determined from measuring the positions of the Bragg peaks.

In order to allow the electron density along the ripple direction to modulate, we include two additional parameters, one to allow for the electron density across the minor side to be different by a ratio f_1 from the electron density across the major side and a second parameter f_2 , which is multiplied by δ functions $\delta(x \pm x_M/2)$ to allow for a different electron density near the kink between the major and the minor sides.

The contour part of the form factor F_C calculated from Eq. (4.38) is plotted in Fig. (4.25).

4.4.2 Transbilayer Part of the Form Factor

Delta function model

Delta function model is described here.

1G and 2G hybrid model

In the hybrid model, the terminal methyl region of the bilayer is represented as a Gaussian function [88]. The headgroups are represented by one and two Gaussian functions in 1G and 2G hybrid model, respectively. The methylene and water regions are each treated as a constant. The gap between the two constants is represented by a sine function. Then, for half of the bilayer, $0 \leq z \leq D/2$, the electron density has

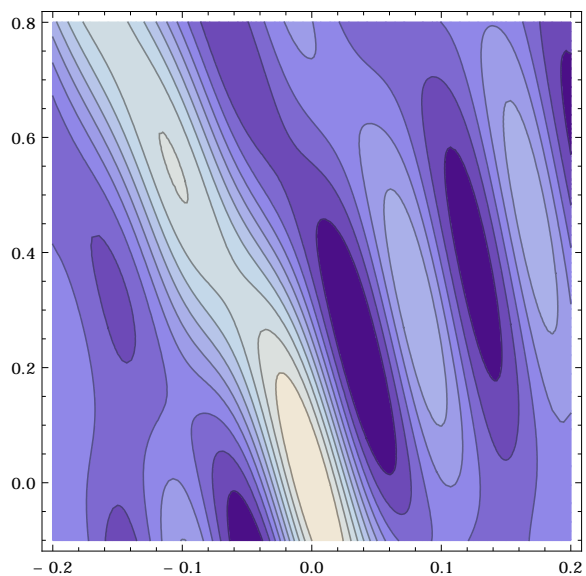


Figure 4.25: Not sure if this plot is useful. The horizontal axis is q_x and the vertical axis is q_z .

the form,

$$\rho(z) = \rho_G(z) + \rho_S(z) + \rho_B(z), \quad (4.39)$$

where the Gaussian part is given by

$$\rho_G(z) = \sum_{i=1}^{1 \text{ or } 2} \rho_{Hi} e^{-(z-Z_{Hi})^2/(2\sigma_{Hi}^2)} + \rho_M e^{-z^2/(2\sigma_M^2)}, \quad (4.40)$$

the strip part is given by

$$\rho_S(z) = \begin{cases} \rho_{CH_2} & \text{for } 0 \leq z < Z_{CH_2}, \\ \rho_W & \text{for } Z_W \leq z \leq D/2, \end{cases} \quad (4.41)$$

and the bridging part is given by

$$\rho_B(z) = \frac{\rho_W - \rho_{CH_2}}{2} \cos \left[\frac{-\pi}{\Delta Z_H} (z - Z_W) \right] + \frac{\rho_W + \rho_{CH_2}}{2} \quad \text{for } Z_{CH_2} < z < Z_W. \quad (4.42)$$

with $\Delta Z_H = Z_W - Z_{CH_2}$. Here, we assume $Z_{H2} > Z_{H1}$. Table 4.5 shows some of the definitions.

	1G	2G
Z_{CH_2}	$Z_{H1} - \sigma_{H1}$	$Z_{H1} - \sigma_{H1}$
Z_W	$Z_{H1} + \sigma_{H1}$	$Z_{H2} + \sigma_{H2}$

Table 4.5: Definitions of Z_{CH_2} and Z_W

The transbilayer profile along $x = -z \tan \psi$ can be obtained by rotating the coordinates x and z by ψ in the clockwise direction and reexpressing $\rho(z)$ in terms of the rotated coordinates. This leads to replacing x with $x' = x \cos \psi + z \sin \psi$ and z with $z' = -x \sin \psi + z \cos \psi$. Then, the rotated transbilayer profile is

$$\rho(x, z) = \delta(x + z \tan \psi)[\rho_G(z') + \rho_S(z') + \rho_B(z')]. \quad (4.43)$$

Taking the two dimensional Fourier transform of Eq. (4.43) leads to the transbi-

layer part of the form factor,

$$F_T = \int_{-\frac{D}{2}}^{\frac{D}{2}} \int_{-\frac{\lambda_r}{2}}^{\frac{\lambda_r}{2}} [\rho(x, z) - \rho_W] e^{i(q_x x + q_z z)} dx dz \quad (4.44)$$

$$= F_G + F_S + F_B. \quad (4.45)$$

The form factor is calculated in the minus fluid convention, where the bilayer electron density is measured with respect to the electron density of the surrounding solvent. The expression for F_T is rather messy, so the derivation and full expression are in the appendix. Here, we note that the fitting parameters in this model are Z_{Hi} , σ_{Hi} , and R_{HiM} for each of the two headgroup Gaussian functions, σ_M for the terminal methyl Gaussian, ΔR for the methylene region, ψ for the lipid tilt, and an overall scaling factor. The contour part of the form factor has four more parameters (A , x_M , f_1 , and f_2). In total, the modified 2G hybrid model implements 14 structural parameters.

4.5 LAXS: results

4.5.1 Data and Electron Density Profile

Table 4.6 and 4.7 summarize observed intensity from data shown in Fig. 4.11. q_z values for observed peaks were corrected for index of refraction (Appendix B.4). We measured scattering on oriented samples in almost identical conditions as the best unoriented sample of Wack and Webb. As discussed earlier, these two types of samples have different Lorentz corrections, so this allowed us to check our data obtained on oriented samples against an unoriented sample. As Table 4.6 shows, agreement between our oriented data and the unoriented data was good, but integrated intensity from our oriented sample was in many cases larger than that from an unoriented sample. We attribute this discrepancy to the way intensity was extracted. In an X-ray data from an oriented sample, each peak was nicely separated, so integrating a peak intensity was trivial. In contrast, some reflections in unoriented data were overlapping with each other (three pairs of overlapping peaks are highlighted in Table 4.6), making separation of intensity difficult. If the (1, 0) peak in the unoriented data were overestimated, that would account for the observed discrepancy. Indeed, the microdensitometer trace in [76] suggests that the (1, 0) and (1, 1) reflections should have similar intensity as we observed.

Show in a table, fitting results. Show an edp. Show the thicknesses of both arms.
Comment on some fine features.

4.6 NGIWAXS: analysis

4.6.1 Absorption Correction

(Under construction)

h	k	q_z (Å $^{-1}$)	q_r (Å $^{-1}$)	I_{hk}^{obs}	box size (pixels)	h	k	q^* (Å $^{-1}$)	oriented $ F_{hk} $	unoriented $ F_{hk} ^*$
1	-1	0.102	-0.043	726	10 \times 7	1	-1	0.111	83.0	60.8
1	0	0.109	0.000	180818	10 \times 7	1	0	0.108	100.0	100.0
1	1	0.114	0.043	241	10 \times 7	1	1	0.123	44.0	26.9
1	3	0.128	0.130	4.8	10 \times 7	1	3	0.185	9.9	7.6
2	-2	0.206	-0.087	51.4	10 \times 7	2	-2	0.224	19.4	15.1
2	-1	0.212	0.044	1818	10 \times 7	2	-1	0.215	80.2	71.2
2	0	0.218	0.000	10200	10 \times 7	2	0	0.217	30.8	39.7
2	1	0.224	0.043	558	10 \times 7	2	1	0.228	42.4	33.9
2	2	0.231	0.086	116	10 \times 7	2	2	0.246	26.8	22.7
2	3	0.23	0.129	27	10 \times 7	2	3	0.271	15.6	14.2
2	4	0.243	0.173	7.6	10 \times 7	2	4	0.301	9.5	7.8
2	5	0.250	0.214	2.9	10 \times 7	2	5	0.329	6.4	
3	-2	0.314	-0.087	305	15 \times 7	3	-2	0.325	36.2	29.3
3	-1	0.321	-0.043	1205	15 \times 7	3	-1	0.322	50.0	44.2
3	0	0.326	0.000	1566	15 \times 7	3	0	0.325	14.4	12.0
3	1	0.333	0.043	31.7	15 \times 7	3	1		7.9	
3	2	0.339	0.086	32.4	15 \times 7	3	2	0.350	11.2	10.5
3	3	0.345	0.129	38.2	15 \times 7	3	3	0.370	14.8	14.9
3	4	0.352	0.172	26.1	15 \times 7	3	4	0.394	13.9	10.0
3	5	0.358	0.215	8.6	15 \times 7	3	5		8.8	

Table 4.6: Observed intensity for $h = 1$ to 3 at $D = 57.8$, $\lambda_r = 145$, and $\gamma = 98.2^\circ$.

*Unoriented data are from Wack and Webb [76].

h	k	q_z (Å $^{-1}$)	q_r (Å $^{-1}$)	I_{hk}^{obs}	box size (pixels)	h	k	oriented $ F_{hk} $
4	-3	0.417	-0.131	143	20 by 8	4	-3	25.7
4	-2	0.423	-0.087	730	20 by 8	4	-2	46.8
4	-1	0.429	-0.043	415	20 by 8	4	-1	24.7
4	0	0.435	0.000	1938	20 by 8	4	0	18.1
4	1			51.5	20 by 8	4	1	8.5
4	2	0.448	0.085	39	20 by 8	4	2	10.4
4	3			weak		4	3	
4	4	0.461	0.173	2.1	20 by 8	4	4	3.4
4	5	0.467	0.215	3.2	20 by 8	4	5	4.6
4	6	0.473	0.259	1.0	20 by 8	4	6	2.8
5	-3	0.525	-0.132	84.4	25 by 9	5	-3	17.3
5	-2	0.532	-0.087	146	25 by 9	5	-2	18.4
5	-1	0.538	-0.042	64.6	25 by 9	5	-1	8.5
5	0	0.544	0.000	259	25 by 9	5	0	7.3
5	1	0.550	0.040	50.2	25 by 9	5	1	7.2
6	-4	0.628	-0.175	10.3	30 by 10	6	-4	6.3
6	-3	0.635	-0.131	13.8	30 by 10	6	-3	6.3
6	-2	0.641	-0.085	9.7	30 by 10	6	-2	4.2
6	-1	0.647	-0.043	2.0	30 by 10	6	-1	0.0
6	0	0.653	0.000	69.0	30 by 10	6	0	4.1
6	1	0.659	0.043	2.5	30 by 10	6	1	0.0
6	2			weak		6	2	weak
6	3	0.672	0.128	42	30 by 10	6	3	10.5
6	4	0.679	0.170	40	30 by 10	6	4	11.7
7	-4	0.737	-0.174	42	35 by 10	7	-4	11.6
7	-3	0.743	-0.130	40	35 by 10	7	-3	9.7
7	-2	0.749	-0.085	15	35 by 10	7	-2	4.8
7	-1	0.755	-0.042	27	35 by 10	7	-1	4.5
7	0	0.760	0.000	41	35 by 10	7	0	3.4
9	-5			weak		9	-5	
9	-4	0.951	-0.174	19	35 by 10	9	-4	
9	-3			weak		9	-3	
9	-2	0.963	-0.085	21.0	35 by 10	9	-2	
9	-1			weak		9	-1	
9	0	0.974	0.000	21.0	35 by 10	9	0	

Table 4.7: Observed intensity for $h = 4$ to 9 at $D = 57.8$, $\lambda_r = 145$, and $\gamma = 98.2^\circ$ (continued from Table 4.6).

4.7 NGIWAXS: model

4.7.1 Thin rod model

4.8 NGIWAXS: results

Figure 4.26 shows near grazing incidence Wide Angle X-ray scattering (NGIWAXS) from an oriented DMPC film in the ripple phase. As can be seen, hydrocarbon chain scattering did not vary considerably between the two D -spacings. A weak feature that looks like an arc coming from the chain peak was observed. This feature extended out from $\phi = 0^\circ$ to at least 70° . This feature might simply be mosaic spread scattering due to the peak near the equator. Because mosaic spread of this sample was very small, it may also be possible that the feature is not mosaic spread arc, but comes from the minor arm, indicating that tilt modulation may occur in the minor arm. Chains are packed quite tightly, unlike in the fluid phase. (I did rocking scan, so show the data, and maybe estimate what scattering would look like based on Lorentzian distribution.)

Figure 4.27 shows an enlarged image of the ripple phase WAXS at $D = 60.8 \text{ \AA}$. We observed a strong peak off the equator and a weak one, the center of which was not determined. The maximum intensity of the strong peak was at $(q_r, q_z) \approx (1.49 \text{ \AA}^{-1}, 0.19 \text{ \AA}^{-1})$ as shown in Fig. 4.28. The weak peak was observed near the equator, but separation of this peak from the strong one was most visible at $q_z = 0.13 \text{ \AA}^{-1}$ as Fig. 4.28 shows. Separation of the two peaks was possible because of the high resolution experiment. In previous runs with the low resolution setup, the ripple peak appeared as a single wide peak.

(some thought) Can we say that the observed arc like scattering is not the mosaic spread, but true sample scattering? Comment on the widths of the peaks observed. Possibly make use of both low and high resolution data. Apply the absorption correction. Show q swaths for various ϕ .

4.9 TWAXS: results

Convert the image to q -space. No strong order on the equator. Compare to NGIWAXS and comment on the absorption effect in NGIWAXS data.

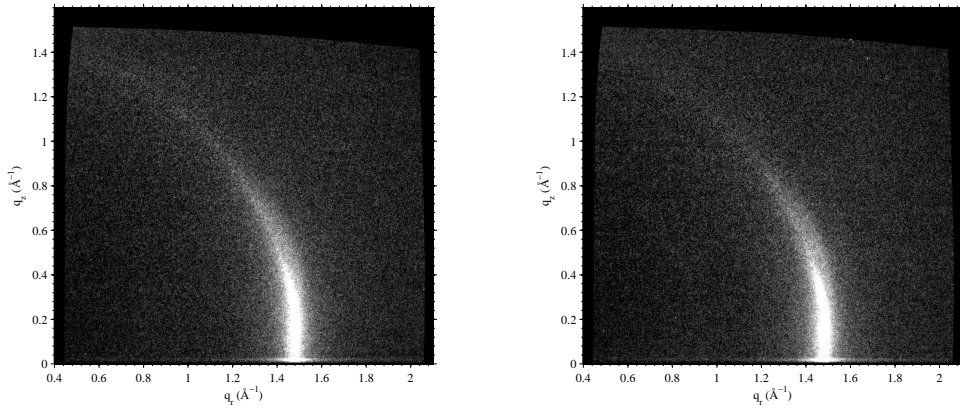


Figure 4.26: NGIWAXS of the DMPC ripple phase for $D = 59.2 \text{ \AA}$ (left) and 60.8 \AA (right). The angle of incidence ω was 0.2° . The black regions around the edge of each image are the q -space that was not probed. The distorted, non rectangular shape of the probed q -space signifies non-linear relation between the CCD space and sample q -space.

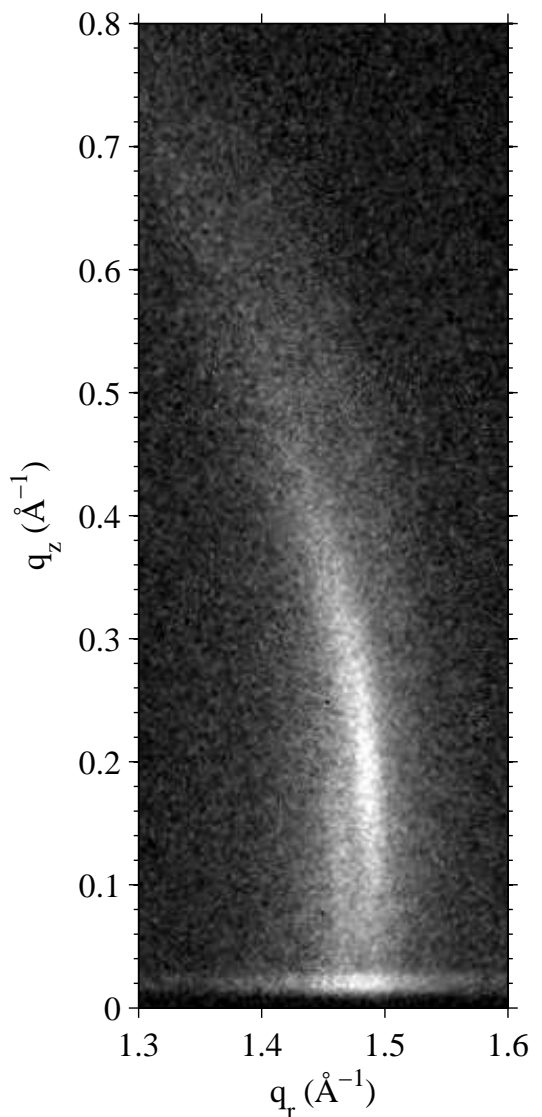


Figure 4.27: Enlarged view of the right image in Fig. 4.26. To show smaller features around the peak, a different contrast is used.

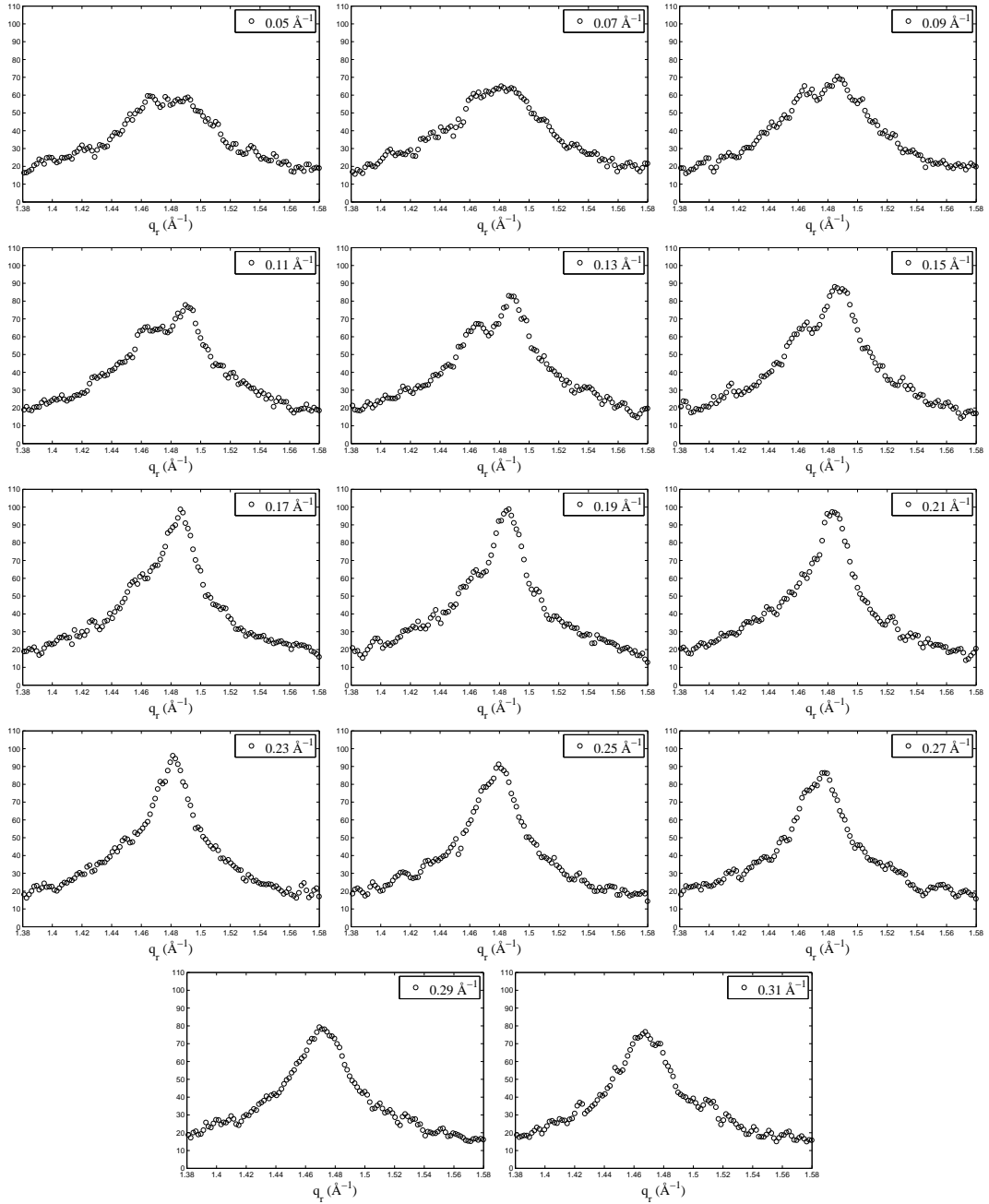


Figure 4.28: q_r swaths, each averaged over 0.02 \AA^{-1} . The center q_z value of a swatch is shown in the figure legends.

4.10 Discussion

Comparison with previous unoriented/oriented stuff.

4.11 Conclusion

Future possible experiments include a high resolution transmission experiment, where both geometric broadening and energy dispersion are minimized. The expected resolution is the width of the X-ray beam, which is about 3 pixels. This experiment doubles the best resolution achieved in this work. Another slightly different high resolution experiment is to use silicon crystal analyzer downstream of the sample, which completely remove geometric broadening. The downside of this type of high resolution experiment is that only one point in q-space is probed at any given exposure, so getting a full 2D map of wide angle scattering is time consuming.

Appendices

Appendix A

Tat

A.1 Analysis of Fixed Angle Data using NFIT

In this section, I propose a slightly new method to analyze the diffuse scattering data. This method may ease measurement of the X-ray form factor at lower q_z ($\leq 0.25 \text{ \AA}^{-1}$).

A.1.1 Theory

A.1.2 Results

A.2 Mosaic Spread for NFIT analysis

First we calculate how mosaic spread affects the structure factor $S(q)$. Next we discuss two experimental methods. Third, we discuss the updated NFIT program. Fourth, we show the results.

A.2.1 Mosaic Spread: Calculation

In this section, an analytical framework for dealing with mosaic spread is developed. A sample of oriented stacks of bilayers consists of many small domains, within which layers are registered in an array. An ideal domain is a domain where the layers are parallel to the substrate, whose surface is in the sample xy -plane, so the orientation \mathbf{n} of an ideal domain is perpendicular to the substrate as shown in Fig. A.1. In general, the orientation \mathbf{n}' of a domain is tilted from that of an ideal domain by some angle α . Then, we consider a mosaic spread distribution function, $P(\alpha)$, representing a

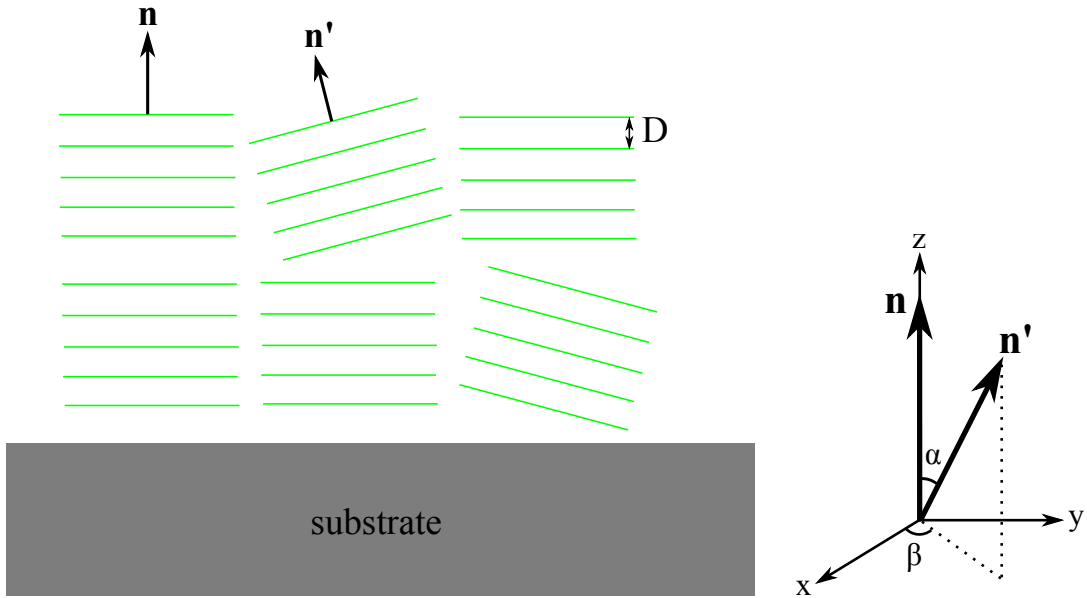


Figure A.1: Two dimensional view of mosaic spread (left) and notations used in this section (right). The stacking direction of an ideal domain is \mathbf{n} and that of a tilted domain \mathbf{n}' . The deviation of \mathbf{n}' from \mathbf{n} denoted as α quantifies the degree of misorientation of a domain. The x , y , and z -axes are the sample coordinates.

probability of finding a domain with a tilt α . We assume that the sample is symmetric about the substrate normal, so that the distribution $P(\alpha)$ does not depend on the azimuthal angle, β . The normalization condition on $P(\alpha)$ is

$$1 = \int_0^{2\pi} d\beta \int_0^{\frac{\pi}{2}} d\alpha \sin \alpha P(\alpha). \quad (\text{A.1})$$

The object of this section is to derive the X-ray scattering structure factor including the distribution function $P(\alpha)$.

First, let us consider a two dimensional example. Our sample consists of two identical domains except a tilt α shown in Fig. A.2. Then, the sample structure factor $S^{\text{sam}}(\mathbf{q})$ is a superposition of the structure factor $S(\mathbf{q})$ of the ideal domain and $S(\mathbf{q}')$ of the tilted domain,

$$S^{\text{sam}}(\mathbf{q}) = S(q_x, q_z) + S(q'_x, q'_z). \quad (\text{A.2})$$

To express $S(q'_x, q'_z)$ in terms of the sample q -space (q_x, q_z) , we write q'_x and q'_z in

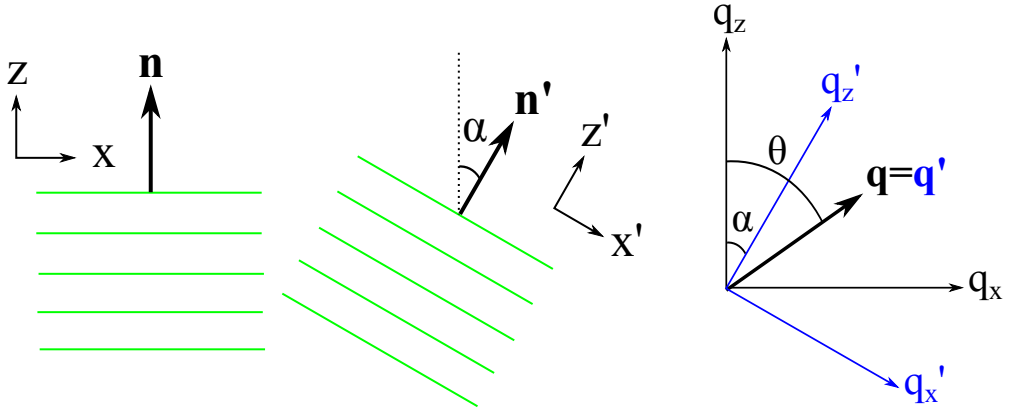


Figure A.2: Example of a two dimensional sample consisting of an ideal and tilted domains. $\mathbf{q} = (q_x, q_z)$ is the sample q -space and $\mathbf{q}' = (q'_x, q'_z)$ is the domain q -space. The two q -spaces are related by a rotation of α about the y -axis, which is into the page.

terms of q_x , q_z , and α ,

$$\begin{aligned} q'_x &= \mathbf{q} \cdot \hat{\mathbf{x}}' = q \cos\left(\frac{\pi}{2} - \theta + \alpha\right) \\ q'_z &= \mathbf{q} \cdot \hat{\mathbf{z}}' = q \sin\left(\frac{\pi}{2} - \theta + \alpha\right) \\ q_x &= q \cos(\pi/2 - \theta) \\ q_z &= q \sin(\pi/2 - \theta) \end{aligned} \quad (\text{A.3})$$

where $q = |\mathbf{q}|$. Eq. (A.2) and (A.3) give the structure factor of a sample consisting of the two domains. With a continuous distribution of \mathbf{n}' , we integrate over the angle α with each structure factor modulated by the distribution function $P(\alpha)$,

$$S_M(\mathbf{q}) = S_M(q, \theta) = \int_{-\frac{\pi}{2}}^{\frac{\pi}{2}} d\alpha S(q'_x, q'_z) P(\alpha), \quad (\text{A.4})$$

Variables q and θ are used in the above equation to make a connection with the three dimensional case, where the spherical coordinates are convenient, which we discuss now.

For a three dimensional sample, the basic idea is the same as the two dimensional case. In the three dimensional case, we also rotate the vector \mathbf{n}' about the z -axis by an angle β after the rotation about the y -axis by an angle α , so all we need to do is to apply appropriate rotation matrices to the sample xyz -axes which define the domain

coordinates $x'y'z'$.

The rotation matrix for rotating a vector about the y -axis is given by

$$R_y = \begin{pmatrix} \cos \alpha & 0 & \sin \alpha \\ 0 & 1 & 0 \\ -\sin \alpha & 0 & \cos \alpha \end{pmatrix} \quad (\text{A.5})$$

and for rotating about the z -axis

$$R_z = \begin{pmatrix} \cos \beta & -\sin \beta & 0 \\ \sin \beta & \cos \beta & 0 \\ 0 & 0 & 1 \end{pmatrix}. \quad (\text{A.6})$$

Then, what we want is

$$\hat{\mathbf{x}}' = R_z R_y \begin{pmatrix} 1 \\ 0 \\ 0 \end{pmatrix} = \begin{pmatrix} \cos \alpha \cos \beta \\ \cos \alpha \sin \beta \\ -\sin \alpha \end{pmatrix} \quad (\text{A.7})$$

$$\hat{\mathbf{y}}' = R_z R_y \begin{pmatrix} 0 \\ 1 \\ 0 \end{pmatrix} = \begin{pmatrix} -\sin \beta \\ \cos \beta \\ 0 \end{pmatrix} \quad (\text{A.8})$$

$$\hat{\mathbf{z}}' = R_z R_y \begin{pmatrix} 0 \\ 0 \\ 1 \end{pmatrix} = \begin{pmatrix} \sin \alpha \cos \beta \\ \sin \alpha \sin \beta \\ \cos \alpha \end{pmatrix}. \quad (\text{A.9})$$

The domain q -space, (q'_x, q'_y, q'_z) , in terms of the sample q -space (q_x, q_y, q_z) is given by

$$q'_x = \mathbf{q} \cdot \hat{\mathbf{x}}' = q_x \cos \alpha \cos \beta + q_y \cos \alpha \sin \beta - q_z \sin \alpha, \quad (\text{A.10})$$

$$q'_y = \mathbf{q} \cdot \hat{\mathbf{y}}' = -q_x \sin \beta + q_y \cos \beta, \quad (\text{A.11})$$

$$q'_z = \mathbf{q} \cdot \hat{\mathbf{z}}' = q_x \sin \alpha \cos \beta + q_y \sin \alpha \sin \beta + q_z \cos \alpha. \quad (\text{A.12})$$

The transformation expressed in the spherical coordinates is

$$\cos \theta' = \frac{q'_z}{q} = \sin \theta \sin \alpha \cos(\phi - \beta) + \cos \theta \cos \alpha, \quad (\text{A.13})$$

$$\tan \phi' = \frac{q'_y}{q'_x} = \frac{\sin \theta \sin(\phi - \beta)}{\sin \theta \cos \alpha \cos(\phi - \beta) - \cos \theta \sin \alpha}. \quad (\text{A.14})$$

Summing over all the domains, we get for the mosaic spread modified structure factor

$$S_M(q, \theta, \phi) = \int_0^{2\pi} d\beta \int_0^{\frac{\pi}{2}} d\alpha S(q, \theta', \phi') P(\alpha) \quad (\text{A.15})$$

with Eq. (A.13) and Eq. (A.14).

To test these equations, let us apply them to the simple case of a stack of rigid layers with their normals parallel to the z -axis in spherical coordinates. The structure factor is then

$$S(q, \theta, \phi) = \frac{\delta(q - \frac{2\pi h}{D})}{q^2} \delta(\cos \theta - 1) \delta(\phi) \quad (\text{A.16})$$

where $\delta(x)$ is the Dirac delta function. From Eq. (A.14), $\delta(\phi')$ is equivalent to $\delta(\beta - \phi)$. Setting $\beta = \phi$ in Eq. (A.13) gives $\cos \theta' = \cos(\alpha - \theta)$. Then, the mosaic spread modified structure factor $S_M(\mathbf{q})$ is

$$\begin{aligned} S_M(q, \theta, \phi) &= \int d\alpha \int d\beta \frac{\delta(q - \frac{2\pi h}{D})}{q^2} \delta(\cos \theta' - 1) \delta(\beta - \phi) P(\alpha) \\ &= \frac{\delta(q - \frac{2\pi h}{D})}{q^2} \int d\alpha \delta(\cos[\alpha - \theta] - 1) P(\alpha) \\ &= \frac{\delta(q - \frac{2\pi h}{D})}{q^2} P(\theta). \end{aligned} \quad (\text{A.17})$$

Eq. (A.17) describes hemispherical shells with radii of $2\pi h/D$ in the sample q -space. As will be described in the next section, a 2D detector records cross sections of these shells, which give rise to mosaic arcs along $q = 2\pi h/D$.

The structure factor of thermally fluctuating layers is not simple delta functions and gives rise to diffuse scattering. Analysis of the diffuse scattering from a sample with mosaic spread requires Eq. (A.15).

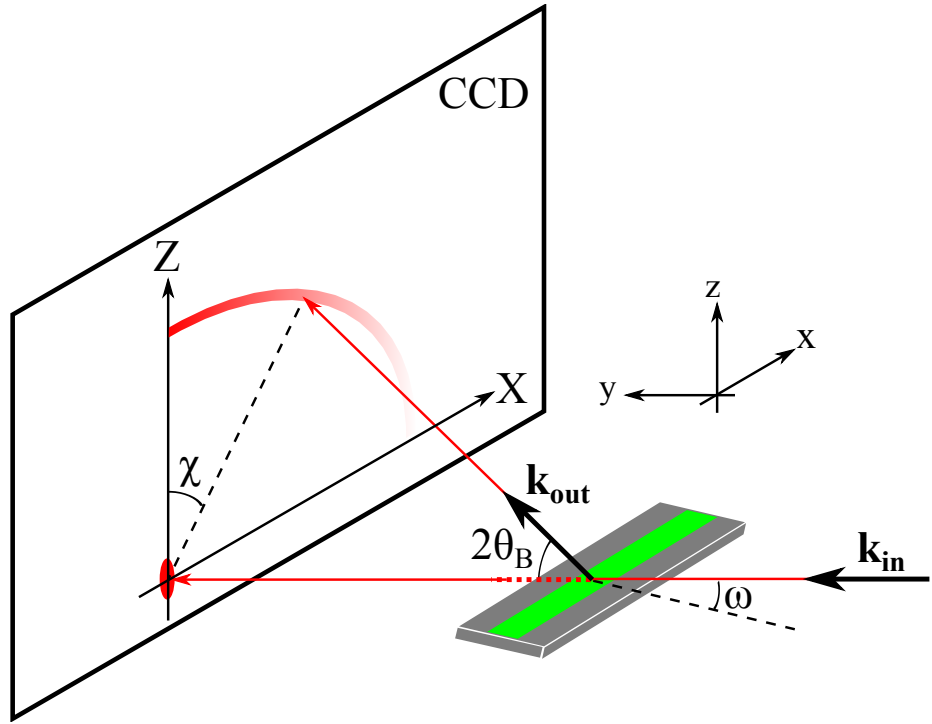


Figure A.3: Notations used in this section. The arc originating from the Z -axis is the mosaic arc due to the mosaic spread distribution.

A.2.2 Mosaic Spread: Near Equivalence of Two Methods

In this section, we discuss experimental procedures to probe appropriate q -space to measure the mosaic spread distribution, $P(\alpha)$. In our setup, the angle of incidence between the beam and substrate, denoted by ω , can be varied. A conventional method to measure $P(\alpha)$ is a rocking scan, where one measures the integrated intensity of a given Bragg peak as a function of ω with a fixed detector position. Another method that takes an advantage of an area detector [89] measures the intensity as a function of χ on a two dimensional detector (see Fig. A.3). This method has been used to quantify complete pole figures for thin films with fiber texture (isotropic in-plane orientation) [90]. First, we want to compare the two methods mentioned above and determine their relationship.

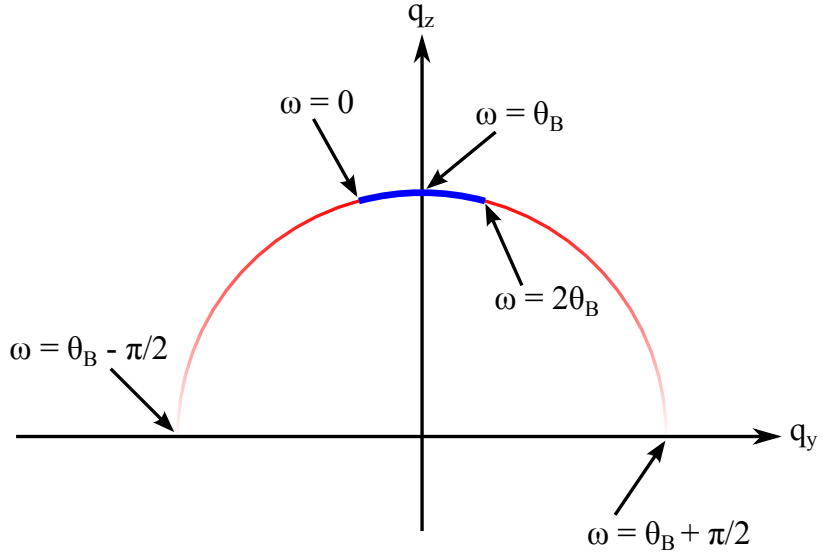


Figure A.4: Rocking scan trace in q -space.

Eq. (4.14) expressed in terms of the coordinates defined in Fig. A.3 is

$$\begin{aligned} q_x &= q \cos \theta \sin \chi \\ q_y &= q (-\sin \theta \cos \omega + \cos \theta \cos \chi \sin \omega) \\ q_z &= q (\sin \theta \sin \omega + \cos \theta \cos \chi \cos \omega). \end{aligned} \quad (\text{A.18})$$

For a rocking scan focused on a particular order, $\chi = 0$ and $\theta = \theta_B$ while ω is varied about θ_B , where θ_B is the Bragg angle. Then,

$$\begin{aligned} q_x &= 0 \\ q_y &= q_B \sin(\omega - \theta_B) \\ q_z &= q_B \cos(\omega - \theta_B), \end{aligned} \quad (\text{A.19})$$

which shows that this scan traces a part of the circular path in the $q_x = 0$ plane as shown in Fig. A.4. As Fig. A.4 shows, however, the rocking scan only probes a small fraction of the entire distribution, limited by $2\theta_B$. As discussed in section 4.3.3, beyond $\omega = 2\theta_B$, the substrate blocks scattering. On the other hand, the ring analysis takes advantage of a two dimensional detector and can probe a substantially wider range of the distribution in principle: approximately $\pm 45^\circ$ at $\omega = \theta_B$. This method is now described.

In the ring method, we set $\omega = \theta_B$ and scan on the detector along $\theta = \theta_B$ as a function of χ . Then, Eq. (A.18) becomes

$$\begin{aligned} q_x &= q \cos \theta_B \sin \chi \\ q_y &= q \sin \theta_B \cos \theta_B (\cos \chi - 1) \\ q_z &= q(\sin^2 \theta_B + \cos^2 \theta_B \cos \chi), \end{aligned} \quad (\text{A.20})$$

where $q = 4\pi \sin \theta_B / \lambda$. For small θ_B , Eq. (A.20) reduces to

$$\begin{aligned} q_x &\approx q \sin \chi \\ q_y &\approx 0 \\ q_z &\approx q \cos \chi. \end{aligned} \quad (\text{A.21})$$

For a sharp Bragg peak, this ring method gives the same mosaic intensity $I(\chi, \theta_B)$ in Eq. (A.21) as the rocking method mosaic intensity $I(\omega - \theta_B)$ in Eq. (A.19) because the mosaic distribution $P(\alpha)$ is in-plane isotropic. Differences occur when diffuse scattering is added. The diffuse scattering intensity is much broader and weaker than the Bragg peaks. In the ring method, it can be estimated as the average from two rings offset on either side from θ_B and subtracted from the θ_B ring.

A.2.3 NFIT

The original NFIT program was written by Dr. Yufeng Liu and described in his thesis. It was used in the Nagle lab, with small updates for data handling, from 2003 until recently. A newer version has been implemented by Michael Jablin that calculates the theoretical structure factor using cylindrical domains appropriate for in-plane correlations [37] rather than rectangular domains appropriate for coherence domains. All these versions approximated the effect of mosaic spread roughly by averaging only in the q_r direction at fixed q_z which means that mosaic rings are approximated as mosaic lines or spikes. The subsequent development described here and not yet adopted by the Nagle lab calculates the structure factor $S(q_r, q_z)$ with rotational symmetry about the z -axis, which eliminates the ϕ' dependence in Eq. (A.15). The program interpolates $S(q_r, q_z)$ in terms of the spherical coordinates q and θ with $\phi = 0$ to perform the double integration in Eq. (A.15). After the mosaic spread

integration, the program performs the q_y integration described in section 3.2.2. For this integration, the calculated S_M is interpolated in terms of q_x , q_y , and q_z .

Note: if the structure factor defined in the Cartesian coordinates is desired (for a case of square domains instead of circular ones), Eq. (A.10 – A.12) can be used instead of Eq. (A.13) and (A.14).

While it is an improvement, the new program also is an approximation because it does not include the unknown form factor $|F(q_z)|$. The mosaic spread integration mixes up intensity at different q_z values, so the separation of $|F(q_z)|$ from $S(\mathbf{q})$ is in principle impossible. One way to deal with this issue would be to combine the SDP program, which determines $|F(q_z)|$, with the NFIT program, but that will end up with too many non-linear parameters. Another possibility is to limit the fitting range to regions close to the meridian. For a small range of integration, it is not unreasonable to assume that the form factor is approximately constant as can be seen from Eq. (A.12) with small q_x , q_y , and α . Therefore, the analysis developed in this appendix ignores the form factor.

A.2.4 Results

A.3 Some More Details of Tat Stuff if needed

Appendix B

Ripple Phase

B.1 Derivation of the contour part of the form factor

In this section, we derive F_C . The ripple profile, $u(x)$ is given by

$$u(x) = \begin{cases} -\frac{A}{\lambda_r - x_0} \left(x + \frac{\lambda_r}{2} \right) & \text{for } -\frac{\lambda_r}{2} \leq x < -\frac{x_0}{2} \\ \frac{A}{x_0} x & \text{for } -\frac{x_0}{2} \leq x \leq \frac{x_0}{2} \\ -\frac{A}{\lambda_r - x_0} \left(x - \frac{\lambda_r}{2} \right) & \text{for } \frac{x_0}{2} < x \leq \frac{\lambda_r}{2} \end{cases} \quad (\text{B.1})$$

The contour part of the form factor is the Fourier transform of the contour function, $C(x, z)$,

$$F_C(\mathbf{q}) = \frac{1}{\lambda_r} \int_{-\frac{\lambda_r}{2}}^{\frac{\lambda_r}{2}} dx \int_{-\frac{D}{2}}^{\frac{D}{2}} dz C(x, z) e^{iq_z z} e^{iq_x x}$$

As discussed in section X, the modulated models allow the electron density to modulate along the ripple direction, x . This means

$$C(x, z) = \begin{cases} f_1 \delta[z - u(x)] & \text{for } -\frac{\lambda_r}{2} \leq x < -\frac{x_0}{2} \\ \delta[z - u(x)] & \text{for } -\frac{x_0}{2} < x < \frac{x_0}{2} \\ f_1 \delta[z - u(x)] & \text{for } \frac{x_0}{2} \leq x < \frac{\lambda_r}{2} \\ + f_2 \delta\left(x + \frac{x_0}{2}\right) \delta\left(z + \frac{A}{2}\right) + f_2 \delta\left(x - \frac{x_0}{2}\right) \delta\left(z - \frac{A}{2}\right). & \end{cases} \quad (\text{B.2})$$

The contribution from the minor arm is

$$\begin{aligned}
& \frac{1}{\lambda_r} \int_{-\frac{\lambda_r}{2}}^{-\frac{x_0}{2}} dx e^{iq_x x} e^{iq_z u(x)} + \int_{\frac{x_0}{2}}^{\frac{\lambda_r}{2}} dx e^{iq_x x} e^{iq_z u(x)} \\
&= \frac{1}{\lambda_r} \int_{\frac{x_0}{2}}^{\frac{\lambda_r}{2}} dx e^{-i[q_x x - q_z \frac{A}{\lambda_r - x_0}(x - \frac{\lambda_r}{2})]} + \int_{\frac{x_0}{2}}^{\frac{\lambda_r}{2}} dx e^{i[q_x x - q_z \frac{A}{\lambda_r - x_0}(x - \frac{\lambda_r}{2})]} \\
&= \frac{2}{\lambda_r} \int_{\frac{x_0}{2}}^{\frac{\lambda_r}{2}} \cos \left[\left(q_x - q_z \frac{A}{\lambda_r - x_0} \right) x + q_z \frac{A}{\lambda_r - x_0} \frac{\lambda_r}{2} \right]
\end{aligned} \tag{B.3}$$

Using a trigonometric identity,

$$\sin u - \sin v = 2 \cos[(u + v)/2] \sin[(u - v)/2],$$

and defining

$$\omega(\mathbf{q}) = \frac{1}{2} (q_x x_0 + q_z A), \tag{B.4}$$

we further simplify Eq. (B.3),

$$\begin{aligned}
&= \frac{2}{\lambda_r} \frac{\lambda_r - x_0}{\frac{1}{2} q_x \lambda_r - \omega} \cos \left[\frac{1}{2} \left(\frac{1}{2} q_x \lambda_r + \omega \right) \right] \sin \left[\frac{1}{2} \left(\frac{1}{2} q_x \lambda_r - \omega \right) \right] \\
&= \frac{1}{\lambda_r} \frac{\lambda_r - x_0}{\frac{1}{2} q_x \lambda_r - \omega} \cos \left[\frac{1}{2} \left(\frac{1}{2} q_x \lambda_r + \omega \right) \right] \frac{\sin \left(\frac{1}{2} q_x \lambda_r - \omega \right)}{\cos \left[\frac{1}{2} \left(\frac{1}{2} q_x \lambda_r - \omega \right) \right]} \\
&= \frac{\lambda_r - x_0}{\lambda_r} \frac{\cos \left[\frac{1}{2} \left(\frac{1}{2} q_x \lambda_r + \omega \right) \right] \sin \left(\frac{1}{2} q_x \lambda_r - \omega \right)}{\cos \left[\frac{1}{2} \left(\frac{1}{2} q_x \lambda_r - \omega \right) \right]} \frac{1}{\frac{1}{2} q_x \lambda_r - \omega}.
\end{aligned} \tag{B.5}$$

Similarly, we calculate the contribution from the major arm,

$$\begin{aligned}
& \frac{1}{\lambda_r} \int_{-\frac{x_0}{2}}^{\frac{x_0}{2}} dx e^{i(q_z A + q_x)x} = \frac{2}{\lambda_r} \int_0^{\frac{x_0}{2}} dx \cos \left(\frac{q_z A}{x_0} + q_x \right) x \\
&= \frac{x_0 \sin \omega}{\lambda_r \omega}
\end{aligned} \tag{B.6}$$

The contribution from the kink region is

$$\begin{aligned}
& \frac{1}{\lambda_r} \iint dx dz \left[\delta \left(x + \frac{x_0}{2} \right) \delta \left(z + \frac{A}{2} \right) + \delta \left(x - \frac{x_0}{2} \right) \delta \left(z - \frac{A}{2} \right) \right] e^{iq_x x} e^{iq_z z} \\
&= \frac{2}{\lambda_r} \cos \omega.
\end{aligned} \tag{B.7}$$

Therefore,

$$F_C(\mathbf{q}) = \frac{x_0 \sin \omega}{\lambda_r - \omega} + f_1 \frac{\lambda_r - x_0}{\lambda_r} \frac{\cos \left[\frac{1}{2} \left(\frac{1}{2} q_x \lambda_r + \omega \right) \right]}{\cos \left[\frac{1}{2} \left(\frac{1}{2} q_x \lambda_r - \omega \right) \right]} \frac{\sin \left(\frac{1}{2} q_x \lambda_r - \omega \right)}{\frac{1}{2} q_x \lambda_r - \omega} + \frac{2f_2}{\lambda_r} \cos \omega \quad (\text{B.8})$$

B.2 Rotation of a Two-Dimensional Function

Let us consider rotating a function, $f(x, z)$ in two dimensions by an angle, ψ , in the counterclockwise direction (see Fig. X). This is easily achieved by rotating the coordinate system by ψ in the clockwise direction. Let rotated coordinates be x' and z' . A point in the original coordinates, (x, z) , is written as (x', z') in the new coordinates. More specifically, the point P is written as $\mathbf{P} = x\hat{\mathbf{x}} + z\hat{\mathbf{z}} = x'\hat{\mathbf{x}}' + z'\hat{\mathbf{z}}'$. $\hat{\mathbf{x}}$ and $\hat{\mathbf{z}}$ in the $x'z'$ coordinate system are written as

$$\hat{\mathbf{x}} = \cos \psi \hat{\mathbf{x}}' + \sin \psi \hat{\mathbf{z}}' \quad (\text{B.9})$$

$$\hat{\mathbf{z}} = -\sin \psi \hat{\mathbf{x}}' + \cos \psi \hat{\mathbf{z}}'. \quad (\text{B.10})$$

Pluggin these in $\mathbf{P} = x\hat{\mathbf{x}} + z\hat{\mathbf{z}}$ leads to

$$x' = x \cos \psi - z \sin \psi \quad (\text{B.11})$$

$$z' = z \cos \psi + x \sin \psi, \quad (\text{B.12})$$

the inverse of which is

$$x = x' \cos \psi + z' \sin \psi \quad (\text{B.13})$$

$$z = -x' \sin \psi + z' \cos \psi. \quad (\text{B.14})$$

Using the latter equations, $f(x, z)$ can be expressed in terms of x' and z' . The resulting function $f(x', z')$ is the rotated version of $f(x, z)$.

As an example, let us consider a Dirac delta function located at $(x, z) = (0, Z_H)$,

that is, $f(x, z) = \delta(x)\delta(z - Z_{\text{H}})$. After the rotation by ψ , it becomes

$$\begin{aligned} f(x, z) &\rightarrow \delta(x \cos \psi + z \sin \psi)\delta(-x \sin \psi + z \cos \psi - Z_{\text{H}}) \\ &= \frac{\delta(x + z \tan \psi)}{|\cos \psi|} \frac{\delta(-x \sin \psi \cos \psi + z \cos^2 \psi - Z_{\text{H} \cos \psi})}{1/|\cos \psi|} \\ &= \delta(x + z \tan \psi)\delta(z \tan \psi \sin \psi \cos \psi + z \cos^2 \psi - Z_{\text{H} \cos \psi}) \\ &= \delta(x + z \tan \psi)\delta(z - Z_{\text{H} \cos \psi}), \end{aligned}$$

which is a part of the expression for $T_\psi(x, z)$ in the simple delta function model.

B.3 Derivation of the transbilayer part of the form factor in the 2G hybrid model

In this section, we derive the trasbilayer part of the form factor calculated from the 2G hybrid model discussed in section X. Defining $z' = -x \sin \psi + z \cos \psi$, the Fourier transform of a Gaussian function along the line tilted from z -axis by ψ is

$$\begin{aligned} &\iint dz dx \rho_{\text{Hi}} \exp\left\{-\frac{(z' - Z_{\text{Hi}})^2}{2\sigma_{\text{Hi}}^2}\right\} \delta(x \cos \psi + z \sin \psi) e^{iq_x x} e^{iq_z z} \\ &= \frac{1}{\cos \psi} \int_{-\frac{D}{2}}^{\frac{D}{2}} dz \rho_{\text{Hi}} \exp\left\{-\frac{(z - Z_{\text{Hi}} \cos \psi)^2}{2\sigma_{\text{Hi}}^2 \cos^2 \psi} + i(q_z - q_x \tan \psi)z\right\} \\ &\approx \rho_{\text{Hi}} \sqrt{2\pi} \sigma_{\text{Hi}} \exp\left\{i\alpha Z_{\text{Hi}} - \frac{1}{2}\alpha^2 \sigma_{\text{Hi}}^2\right\} \end{aligned} \quad (\text{B.15})$$

with $\alpha = q_z \cos \psi - q_x \sin \psi$. Using Eq. (B.15) and adding the other side of the bilayer and the terminal methyl term, we get

$$\begin{aligned} F_{\text{G}} &= \sqrt{2\pi} \left[-\rho_{\text{M}} \sigma_{\text{M}} \exp\left\{-\frac{1}{2}\alpha^2 \sigma_{\text{M}}^2\right\} \right. \\ &\quad \left. + \sum_{i=1}^{1 \text{ or } 2} 2\rho_{\text{Hi}} \sigma_{\text{Hi}} \cos(\alpha Z_{\text{Hi}}) \exp\left\{-\frac{1}{2}\alpha^2 \sigma_{\text{Hi}}^2\right\} \right]. \end{aligned} \quad (\text{B.16})$$

The strip part of the model in the minus fluid convention is

$$\rho_S(z) = \begin{cases} -\Delta\rho & \text{for } 0 \leq z < Z_{CH_2} \cos \psi, \\ 0 & \text{for } Z_W \cos \psi \leq z \leq D/2, \end{cases} \quad (B.17)$$

where $\Delta\rho = \rho_W - \rho_{CH_2}$. Then, the corresponding Fourier transform is

$$\begin{aligned} F_S &= \iint dz dx e^{iq_x x} e^{iq_z z} \rho_S(z) \delta(x \cos \psi + z \sin \psi) \\ &= \frac{2}{\cos \psi} \int_0^{Z_{CH_2} \cos \psi} dz \cos\left(\frac{\alpha}{\cos \psi} z\right) (-\Delta\rho) \\ &= -2\Delta\rho \frac{\sin(\alpha Z_{CH_2})}{\alpha}. \end{aligned} \quad (B.18)$$

The bridging part of the model in the minus fluid convention is

$$\rho_B(x, z) = \frac{\Delta\rho}{2} \cos\left[\frac{-\pi}{\Delta Z_H}(z' - Z_W)\right] - \frac{\Delta\rho}{2} \quad (B.19)$$

for $Z_{CH_2} \cos \psi < z < Z_W \cos \psi$, and 0 otherwise. Here, $\Delta Z_H = Z_W - Z_{CH_2}$. Then, for the strip part of the form factor, we have

$$\begin{aligned} F_B &= \iint dz dx e^{iq_x x} e^{iq_z z} \delta(x \cos \psi + z \sin \psi) \rho_B(x, z) \\ &= \frac{\Delta\rho}{\cos \psi} \int_{Z_{CH_2} \cos \psi}^{Z_W \cos \psi} dz \cos\left(\alpha \frac{z}{\cos \psi}\right) \left\{ \cos\left[-\frac{\pi}{\Delta Z_H} \left(\frac{z}{\cos \psi} - Z_W\right)\right] - 1 \right\} \\ &= \Delta\rho \left\{ \frac{\Delta Z_H \sin\left[\frac{\pi(-u+Z_W)}{\Delta Z_H} + \alpha u\right]}{-2\pi + 2\alpha \Delta Z_H} + \frac{\Delta Z_H \sin\left[\frac{\pi(u-Z_W)}{\Delta Z_H} + \alpha u\right]}{2\pi + 2\alpha \Delta Z_H} - \frac{\sin(\alpha u)}{\alpha} \right\} \Big|_{Z_{CH_2}}^{Z_W} \\ &= -\frac{\Delta\rho}{\alpha} [\sin(\alpha Z_W) - \sin(\alpha Z_{CH_2})] \\ &\quad + \frac{\Delta\rho}{2} \left(\frac{1}{\alpha + \frac{\pi}{\Delta Z_H}} + \frac{1}{\alpha - \frac{\pi}{\Delta Z_H}} \right) [\sin(\alpha Z_W) + \sin(\alpha Z_{CH_2})]. \end{aligned} \quad (B.20)$$

Because our X-ray scattering intensity was measured in a relative scale, an overall scaling factor was necessary for a non linear least square fitting procedure. This means that $\Delta\rho$ can be absorbed in the scaling factor. Doing so means that the values of ρ_{Hi} and ρ_M resulting from a fitting procedure are relative to $\Delta\rho$. One way to have these parameters in the absolute scale is to integrate the bilayer electron density over

the lipid volume and equate the result to the total number of electrons in the lipid, which can easily be calculated from the chemical formula. For the ripple phase study in this thesis, the absolute values of the electron density were not of importance, so the discussion was omitted in the main text.

B.4 Correction due to refractive index

q_z needs to be corrected for index of refraction [39].

Let θ' and λ' be the true scattering angle and wavelength within the sample. The wavelength by an energy analyzer, λ , and the scattering angle calculated from a position on a CCD detector, θ are apparent. The correction is not necessary in the horizontal direction. The Snell's law in Fig. X gives

$$n \cos \theta = n' \cos \theta' \quad (\text{B.21})$$

$$n\lambda = n'\lambda'. \quad (\text{B.22})$$

For low angle X-ray scattering, the momentum transfer along z direction is

$$q_z = \frac{4\pi \sin \theta'}{\lambda'} \quad (\text{B.23})$$

$$= \frac{4\pi n'}{n\lambda} \sin \theta' \quad (\text{B.24})$$

$$= \frac{4\pi n'}{n\lambda} \sqrt{1 - \cos^2 \theta'} \quad (\text{B.25})$$

$$= \frac{4\pi n'}{n\lambda} \sqrt{1 - \left(\frac{n}{n'} \cos \theta\right)^2}. \quad (\text{B.26})$$

The apparent scattering angle, θ , is directly related to the vertical pixel position, p_z , by

$$\theta = \frac{1}{2} \tan^{-1} \left(\frac{p_z}{S} \right), \quad (\text{B.27})$$

where S is the sample-to-detector distance. The typical units of S and p_z are in mm. In our experimental setup, $n = 1$ and $n' = 0.9999978$ for lipids at $\lambda = 1.18 \text{ \AA}$. $S = 359.7 \text{ mm}$.

Bibliography

- [1] Martin J. Janiak, Donald M. Small, and G. Graham Shipley. Nature of the thermal pretransition of synthetic phospholipids: dimyristoyl- and dipalmitoyl-lecithin. *Biochemistry*, 15(21):4575–4580, 1976.
- [2] Rainer Fischer, Mariola Fotin-Mleczek, Hansjrg Hufnagel, and Roland Brock. Break on through to the other sidebiophysics and cell biology shed light on cell-penetrating peptides. *ChemBioChem*, 6(12):2126–2142, 2005.
- [3] Alain Joliot and Alain Prochiantz. Transduction peptides: from technology to physiology. *Nat Cell Biol*, 6(3), 2004.
- [4] Maria Lindgren, Mattias Hllbrink, Alain Prochiantz, and lo Langel. Cell-penetrating peptides. *Trends in Pharmacological Sciences*, 21(3):99 – 103, 2000.
- [5] Alan D. Frankel and Carl O. Pabo. Cellular uptake of the tat protein from human immunodeficiency virus. *Cell*, 55(6):1189 – 1193, 1988.
- [6] Maurice Green and Paul M. Loewenstein. Autonomous functional domains of chemically synthesized human immunodeficiency virus tat trans-activator protein. *Cell*, 55(6):1179 – 1188, 1988.
- [7] Eric Vifs, Priscille Brodin, and Bernard Lebleu. Hiv-1 tat protein basic domain rapidly translocates through the plasma membrane and accumulates in the cell nucleus. *Journal of Biological Chemistry*, 272(25):16010–16017, 1997.
- [8] Gohar Ter-Avetisyan, Gisela Tnnemann, Danny Nowak, Matthias Nitschke, Andreas Herrmann, Marek Drab, and M. Cristina Cardoso. Cell entry of arginine-rich peptides is independent of endocytosis. *Journal of Biological Chemistry*, 284(6):3370–3378, 2009.

- [9] Gisela Tnnemann, Robert M. Martin, Simone Haupt, Christoph Patsch, Frank Edenhofer, and M. Cristina Cardoso. Cargo-dependent mode of uptake and bioavailability of tat-containing proteins and peptides in living cells. *The FASEB Journal*, 20(11):1775–1784, 2006.
- [10] Andr Ziegler, Pierluigi Nervi, Markus Drrenberger, and Joachim Seelig. The cationic cell-penetrating peptide cpptat derived from the hiv-1 protein tat is rapidly transported into living fibroblasts: optical, biophysical, and metabolic evidence. *Biochemistry*, 44(1):138–148, 2005. PMID: 15628854.
- [11] J. S. Wadia, R. V. Stan, and S. F. Dowdy. Transducible tat-ha fusogenic peptide enhances escape of tat-fusion proteins after lipid raft macropinocytosis. *Nature Medicine*, 10(3):310–315, 2004.
- [12] I. M. Kaplan, J. S. Wadia, and S. F. Dowdy. Cationic tat peptide transduction domain enters cells by macropinocytosis. *Journal of Controlled Release*, 102(1):247–253, 2005.
- [13] David A Mann and Alan D Frankel. Endocytosis and targeting of exogenous hiv-1 tat protein. *The EMBO journal*, 10(7):1733, 1991.
- [14] Jean Philippe Richard, Kamran Melikov, Hilary Brooks, Paul Prevot, Bernard Lebleu, and Leonid V Chernomordik. Cellular uptake of unconjugated tat peptide involves clathrin-dependent endocytosis and heparan sulfate receptors. *Journal of Biological Chemistry*, 280(15):15300–15306, 2005.
- [15] Simon W Jones, Richard Christison, Ken Bundell, Catherine J Voyce, Sarah Brockbank, Peter Newham, and Mark A Lindsay. Characterisation of cell-penetrating peptide-mediated peptide delivery. *British journal of pharmacology*, 145(8):1093–1102, 2005.
- [16] Agnès Vendeville, Fabienne Rayne, Anne Bonhoure, Nadir Bettache, Philippe Montcourier, and Bruno Beaumelle. Hiv-1 tat enters t cells using coated pits before translocating from acidified endosomes and eliciting biological responses. *Molecular biology of the cell*, 15(5):2347–2360, 2004.
- [17] Christina Foerg, Urs Ziegler, Jimena Fernandez-Carneado, Ernest Giralt, Robert Rennert, Annette G Beck-Sickinger, and Hans P Merkle. Decoding the entry of

- two novel cell-penetrating peptides in hela cells: lipid raft-mediated endocytosis and endosomal escape. *Biochemistry*, 44(1):72–81, 2005.
- [18] Antonio Fittipaldi and Mauro Giacca. Transcellular protein transduction using the tat protein of hiv-1. *Advanced drug delivery reviews*, 57(4):597–608, 2005.
 - [19] Ying Liu, Melina Jones, Cynthia M Hingtgen, Guojun Bu, Nick Laribee, Rudolph E Tanzi, Robert D Moir, Avindra Nath, and Johnny J He. Uptake of hiv-1 tat protein mediated by low-density lipoprotein receptor-related protein disrupts the neuronal metabolic balance of the receptor ligands. *Nature medicine*, 6(12):1380–1387, 2000.
 - [20] Vladimir P Torchilin, Ram Rammohan, Volkmar Weissig, and Tatyana S Levchenko. Tat peptide on the surface of liposomes affords their efficient intracellular delivery even at low temperature and in the presence of metabolic inhibitors. *Proceedings of the National Academy of Sciences*, 98(15):8786–8791, 2001.
 - [21] Vladimir P Torchilin, Tatyana S Levchenko, Ram Rammohan, Natalia Volodina, Brigitte Papahadjopoulos-Sternberg, and Gerard GM D’Souza. Cell transfection in vitro and in vivo with nontoxic tat peptide-liposome–dna complexes. *Proceedings of the National Academy of Sciences*, 100(4):1972–1977, 2003.
 - [22] Carsten Rudolph, Christian Plank, James Lausier, Ulrike Schillinger, Rainer H Müller, and Joseph Rosenecker. Oligomers of the arginine-rich motif of the hiv-1 tat protein are capable of transferring plasmid dna into cells. *Journal of Biological Chemistry*, 278(13):11411–11418, 2003.
 - [23] Ashok Chauhan, Akshay Tikoo, Arvinder K Kapur, and Mahavir Singh. The taming of the cell penetrating domain of the hiv tat: myths and realities. *Journal of Controlled Release*, 117(2):148–162, 2007.
 - [24] JM Sabatier, E Vives, K Mabrouk, ABDELAZIZ Benjouad, H Rochat, A Duval, B Hue, and ELMOSTAFA Bahraoui. Evidence for neurotoxic activity of tat from human immunodeficiency virus type 1. *Journal of virology*, 65(2):961–967, 1991.
 - [25] A. Mishra, V. D. Gordon, L. H. Yang, R. Coridan, and G. C. L. Wong. Hiv tat forms pores in membranes by inducing saddle-splay curvature: Potential

- role of bidentate hydrogen bonding. *Angewandte Chemie-International Edition*, 47(16):2986–2989, 2008.
- [26] S. T. Yang, E. Zaitseva, L. V. Chernomordik, and K. Melikov. Cell-penetrating peptide induces leaky fusion of liposomes containing late endosome-specific anionic lipid. *Biophysical Journal*, 99(8):2525–2533, 2010.
- [27] P. E. G. Thoren, D. Persson, E. K. Esbjorner, M. Goksor, P. Lincoln, and B. Norden. Membrane binding and translocation of cell-penetrating peptides. *Biochemistry*, 43(12):3471–3489, 2004.
- [28] SD Krämer and H Wunderli-Allenspach. No entry for tat (44–57) into liposomes and intact mdck cells: novel approach to study membrane permeation of cell-penetrating peptides. *Biochimica et Biophysica Acta (BBA)-Biomembranes*, 1609(2):161–169, 2003.
- [29] C. Ciobanasu, J. P. Siebrasse, and U. Kubitscheck. Cell-penetrating hiv1 tat peptides can generate pores in model membranes. *Biophysical Journal*, 99(1):153–62, 2010.
- [30] Philip A Gurnev, Sung-Tae Yang, Kamran C Melikov, Leonid V Chernomordik, and Sergey M Bezrukov. Cationic cell-penetrating peptide binds to planar lipid bilayers containing negatively charged lipids but does not induce conductive pores. *Biophysical journal*, 104(9):1933–1939, 2013.
- [31] H. D. Herce, A. E. Garcia, J. Litt, R. S. Kane, P. Martin, N. Enrique, A. Rebollo, and V. Milesi. Arginine-rich peptides destabilize the plasma membrane, consistent with a pore formation translocation mechanism of cell-penetrating peptides. *Biophysical Journal*, 97(7):1917–1925, 2009.
- [32] Y. C. Su, A. J. Waring, P. Ruchala, and M. Hong. Membrane-bound dynamic structure of an arginine-rich cell-penetrating peptide, the protein transduction domain of hiv tat, from solid-state nmr. *Biochemistry*, 49(29):6009–6020, 2010.
- [33] S. Shojania and J. D. O’Neil. Hiv-1 tat is a natively unfolded protein - the solution conformation and dynamics of reduced hiv-1 tat-(1-72) by nmr spectroscopy. *Journal of Biological Chemistry*, 281(13):8347–8356, 2006.

- [34] P. Bayer, M. Kraft, A. Ejchart, M. Westendorp, R. Frank, and P. Rosch. Structural studies of hiv-1 tat protein. *Journal of Molecular Biology*, 247(4):529–535, 1995.
- [35] H. D. Herce and A. E. Garcia. Molecular dynamics simulations suggest a mechanism for translocation of the hiv-1 tat peptide across lipid membranes. *Proceedings of the National Academy of Sciences of the United States of America*, 104(52):20805–20810, 2007.
- [36] S. Yesylevskyy, S. J. Marrink, and A. E. Mark. Alternative mechanisms for the interaction of the cell-penetrating peptides penetratin and the tat peptide with lipid bilayers. *Biophysical Journal*, 97(1):40–49, 2009.
- [37] Y. Lyatskaya, Y. F. Liu, S. Tristram-Nagle, J. Katsaras, and J. F. Nagle. Method for obtaining structure and interactions from oriented lipid bilayers. *Physical Review E*, 63(1):0119071–0119079, 2001.
- [38] Y. F. Liu and J. F. Nagle. Diffuse scattering provides material parameters and electron density profiles of biomembranes. *Physical Review E*, 69(4):040901–040904(R), 2004.
- [39] Yufeng Liu. *NEW METHOD TO OBTAIN STRUCTURE OF BIOMEMBRANES USING DIFFUSE -RAY SCATTERING: APPLICATION TO FLUID PHASE DOPC LIPID BILAYERS*. PhD thesis, Carnegie Mellon University, 2003.
- [40] John F Nagle and Stephanie Tristram-Nagle. Structure of lipid bilayers. *Biochimica et Biophysica Acta (BBA)-Reviews on Biomembranes*, 1469(3):159–195, 2000.
- [41] Norbert Kuerka, John F. Nagle, Jonathan N. Sachs, Scott E. Feller, Jeremy Pencer, Andrew Jackson, and John Katsaras. Lipid bilayer structure determined by the simultaneous analysis of neutron and x-ray scattering data. *Biophysical Journal*, 95(5):2356 – 2367, 2008.
- [42] Stephanie Tristram-Nagle, Yufeng Liu, Justin Legleiter, and John F. Nagle. Structure of gel phase DMPC determined by x-ray diffraction. *Biophysical Journal*, 83(6):3324 – 3335, 2002.

- [43] Anthony R. Braun, Jonathan N. Sachs, and John F. Nagle. Comparing simulations of lipid bilayers to scattering data: The gromos 43a1-s3 force field. *The Journal of Physical Chemistry B*, 117(17):5065–5072, 2013.
- [44] <http://seal.web.cern.ch/seal/documents/minuit/mnusersguide.pdf>.
- [45] <http://lcgapp.cern.ch/project/cls/work-packages/mathlibs/minuit/index.html>.
- [46] Berk Hess, Carsten Kutzner, David van der Spoel, and Erik Lindahl. Gromacs 4: Algorithms for highly efficient, load-balanced, and scalable molecular simulation. *Journal of Chemical Theory and Computation*, 4(3):435–447, 2008.
- [47] Joakim P. M. Jmbeck and Alexander P. Lyubartsev. Derivation and systematic validation of a refined all-atom force field for phosphatidylcholine lipids. *The Journal of Physical Chemistry B*, 116(10):3164–3179, 2012.
- [48] Joakim P. M. Jmbeck and Alexander P. Lyubartsev. An extension and further validation of an all-atomistic force field for biological membranes. *Journal of Chemical Theory and Computation*, 8(8):2938–2948, 2012.
- [49] Viktor Hornak, Robert Abel, Asim Okur, Bentley Strockbine, Adrian Roitberg, and Carlos Simmerling. Comparison of multiple amber force fields and development of improved protein backbone parameters. *Proteins: Structure, Function, and Bioinformatics*, 65(3):712–725, 2006.
- [50] W. L. Jorgensen, J. Chandrasekhar, J. D. Madura, R. W. Impey, and M. L. Klein. Comparison of simple potential functions for simulating liquid water. *Journal of Chemical Physics*, 79(2):926–935, 1983.
- [51] Norbert Kuerka, John Katsaras, and JohnF. Nagle. Comparing membrane simulations to scattering experiments: Introducing the simtoexp software. *Journal of Membrane Biology*, 235(1):43–50, 2010.
- [52] Shuichi Miyamoto and Peter A Kollman. Settle: an analytical version of the shake and rattle algorithm for rigid water models. *Journal of computational chemistry*, 13(8):952–962, 1992.

- [53] B. Hess, H. Bekker, H. J. C. Berendsen, and J. G. E. M. Fraaije. Lincs: A linear constraint solver for molecular simulations. *J Comput Chem*, 18(12):1463–1472, 1997.
- [54] Tom Darden, Darrin York, and Lee Pedersen. Particle mesh ewald: An $n \log(n)$ method for ewald sums in large systems. *The Journal of chemical physics*, 98(12):10089–10092, 1993.
- [55] Giovanni Bussi, Davide Donadio, and Michele Parrinello. Canonical sampling through velocity rescaling. *The Journal of chemical physics*, 126(1):014101, 2007.
- [56] Michele Parrinello and Aneesur Rahman. Polymorphic transitions in single crystals: A new molecular dynamics method. *Journal of Applied physics*, 52(12):7182–7190, 1981.
- [57] Norbert Kučerka, Yufeng Liu, Nanjun Chu, Horia I Petrache, Stephanie Tristram-Nagle, and John F Nagle. Structure of fully hydrated fluid phase DMPC and DLPC lipid bilayers using X-ray scattering from oriented multilamellar arrays and from unilamellar vesicles. *Biophysical journal*, 88(4):2626–2637, 2005.
- [58] Norbert Kučerka, Stephanie Tristram-Nagle, and John F Nagle. Closer look at structure of fully hydrated fluid phase dppc bilayers. *Biophysical journal*, 90(11):L83–L85, 2006.
- [59] Norbert Kučerka, Stephanie Tristram-Nagle, and John F Nagle. Structure of fully hydrated fluid phase lipid bilayers with monounsaturated chains. *The Journal of membrane biology*, 208(3):193–202, 2005.
- [60] Stephanie Tristram-Nagle, Chao-Ping Yang, and John F Nagle. Thermodynamic studies of purple membrane. *Biochimica et Biophysica Acta (BBA)-Biomembranes*, 854(1):58–66, 1986.
- [61] <http://www.basic.northwestern.edu/biotools/proteincalc.html>.
- [62] A. C. V. Johansson and E. Lindahl. The role of lipid composition for insertion and stabilization of amino acids in membranes. *Journal of Chemical Physics*, 130(18), 2009.

- [63] S. Tristram-Nagle and J. F. Nagle. Hiv-1 fusion peptide decreases bending energy and promotes curved fusion intermediates. *Biophysical Journal*, 93(6):2048–2055, 2007.
- [64] L. B. Li, I. Vorobyov, and T. W. Allen. Potential of mean force and pk(a) profile calculation for a lipid membrane-exposed arginine side chain. *Journal of Physical Chemistry B*, 112(32):9574–9587, 2008.
- [65] I. Vorobyov, L. B. Li, and T. W. Allen. Assessing atomistic and coarse-grained force fields for protein-lipid interactions: The formidable challenge of an ionizable side chain in a membrane. *Journal of Physical Chemistry B*, 112(32):9588–9602, 2008.
- [66] J. L. MacCallum, W. F. D. Bennett, and D. P. Tieleman. Distribution of amino acids in a lipid bilayer from computer simulations. *Biophysical Journal*, 94(9):3393–3404, 2008.
- [67] E. V. Schow, J. A. Freites, P. Cheng, A. Bernsel, G. von Heijne, S. H. White, and D. J. Tobias. Arginine in membranes: The connection between molecular dynamics simulations and translocon-mediated insertion experiments. *Journal of Membrane Biology*, 239(1-2):35–48, 2011.
- [68] W. C. Wimley, T. P. Creamer, and S. H. White. Solvation energies of amino acid side chains and backbone in a family of host-guest pentapeptides. *Biochemistry*, 35(16):5109–5124, 1996.
- [69] W. C. Wimley and S. H. White. Experimentally determined hydrophobicity scale for proteins at membrane interfaces. *Nature Structural Biology*, 3(10):842–848, 1996.
- [70] B. Roux. Lonely arginine seeks friendly environment. *Journal of General Physiology*, 130(2):233–236, 2007.
- [71] W. Kabsch and C. Sander. Dictionary of protein secondary structure: pattern recognition of hydrogen-bonded and geometrical features. *Biopolymers*, 22(12):2577–637, 1983.
- [72] D. Choi, J. H. Moon, H. Kim, B. J. Sung, M. W. Kim, G. Y. Tae, S. K. Satija, B. Akgun, C. J. Yu, H. W. Lee, D. R. Lee, J. M. Henderson, J. W. Kwong,

- K. L. Lam, K. Y. C. Lee, and K. Shin. Insertion mechanism of cell-penetrating peptides into supported phospholipid membranes revealed by x-ray and neutron reflection. *Soft Matter*, 8(32):8294–8297, 2012.
- [73] K. Huang and A. E. Garcia. Free energy of translocating an arginine-rich cell-penetrating peptide across a lipid bilayer suggests pore formation. *Biophysical Journal*, 104(2):412–420, 2013.
- [74] Martin J Janiak, Donald M Small, and G Graham Shipley. Temperature and compositional dependence of the structure of hydrated dimyristoyl lecithin. *Journal of Biological Chemistry*, 254(13):6068–6078, 1979.
- [75] A. Tardieu, Vittorio Luzzati, and F.C. Reman. Structure and polymorphism of the hydrocarbon chains of lipids: A study of lecithin-water phases. *Journal of Molecular Biology*, 75(4):711 – 733, 1973.
- [76] Daniel C. Wack and Watt W. Webb. Synchrotron x-ray study of the modulated lamellar phase $p\beta'$ in the lecithin-water system. *Phys. Rev. A*, 40:2712–2730, Sep 1989.
- [77] Haruhiko Yao, Sinzi Matuoka, Boris Tenchov, and Ichiro Hatta. Metastable ripple phase of fully hydrated dipalmitoylphosphatidylcholine as studied by small angle x-ray scattering. *Biophysical journal*, 59(1):252–255, 1991.
- [78] W J Sun, S Tristram-Nagle, R M Suter, and J F Nagle. Structure of the ripple phase in lecithin bilayers. *Proceedings of the National Academy of Sciences*, 93(14):7008–7012, 1996.
- [79] Beth A Cunningham, Ari-David Brown, David H Wolfe, W Patrick Williams, and Anthony Brain. Ripple phase formation in phosphatidylcholine: Effect of acyl chain relative length, position, and unsaturation. *Physical Review E*, 58(3):3662, 1998.
- [80] Kell Mortensen, Walter Pfeiffer, Erich Sackmann, and Wolfgang Knoll. Structural properties of a phosphatidylcholine-cholesterol system as studied by small-angle neutron scattering: ripple structure and phase diagram. *Biochimica et Biophysica Acta (BBA)-Biomembranes*, 945(2):221–245, 1988.

- [81] Jeremy P Bradshaw, Michael S Edenborough, Philip JH Sizer, and Anthony Watts. Observation of rippled dioleoylphosphatidylcholine bilayers by neutron diffraction. *Biochimica et Biophysica Acta (BBA)-Biomembranes*, 987(1):111–114, 1989.
- [82] JT Woodward IV and JA Zasadzinski. Amplitude, wave form, and temperature dependence of bilayer ripples in the p β phase. *Physical Review E*, 53(4):R3044, 1996.
- [83] JA Zasadzinski, J Schneir, J Gurley, V Elings, and PK Hansma. Scanning tunneling microscopy of freeze-fracture replicas of biomembranes. *Science*, 239(4843):1013–1015, 1988.
- [84] M. P. Hentschel and F. Rustichelli. Structure of the ripple phase P'_β in hydrated phosphatidylcholine multilamellar membranes. *Phys. Rev. Lett.*, 66:903–906, Feb 1991.
- [85] Alex H. de Vries, Serge Yefimov, Alan E. Mark, and Siewert J. Marrink. Molecular structure of the lecithin ripple phase. *Proceedings of the National Academy of Sciences of the United States of America*, 102(15):5392–5396, 2005.
- [86] S. A. Tristram-Nagle. Preparation of oriented, fully hydrated lipid samples for structure determination using x-ray scattering. *Methods Mol Biol*, 400:63–75, 2007.
- [87] http://henke.lbl.gov/optical_constants.
- [88] M.C. Wiener, R.M. Suter, and J.F. Nagle. Structure of the fully hydrated gel phase of dipalmitoylphosphatidylcholine. *Biophysical Journal*, 55(2):315 – 325, 1989.
- [89] Alejandro B. Rodriguez-Navarro. Registering pole figures using an X-ray single-crystal diffractometer equipped with an area detector. *Journal of Applied Crystallography*, 40(3):631–634, Jun 2007.
- [90] Jessy L. Baker, Leslie H. Jimison, Stefan Mannsfeld, Steven Volkman, Shong Yin, Vivek Subramanian, Alberto Salleo, A. Paul Alivisatos, and Michael F. Toney. Quantification of thin film crystallographic orientation using x-ray diffraction with an area detector. *Langmuir*, 26(11):9146–9151, 2010. PMID: 20361783.